Università degli studi di Padova

FACOLTÀ DI INGEGNERIA
DIPARTIMENTO DI INGEGNERIA INDUSTRIALE
Corso di Laurea Magistrale in Ingegneria Aerospaziale

Numerical study of the erosion of a porous solid layer in a channel flow

Relatore:
Prof. Francesco Picano
Correlatore:
Ing. Federico Dalla Barba

Laureando: **Silvia Tumelero**
1236485

Anno Accademico 2022/2023

A mia madre e a mio padre

che hanno sempre creduto in me,

per avermi sostenuto e accompagnato

nei momenti più difficili di questo percorso.

Abstract

Fluid-structure interaction (FSI) is a strongly nonlinear problem involving the interaction between the governing equations of fluid dynamics and solid mechanics. The FSI problem can be found in several scientific fields, ranging from civil, aeronautical, and biomedical engineering to geotechnics. FSI involves multi-physics phenomena and becomes more complex when crack initialization and fracture (e.g. hydraulic fracturing) are taken into account. The solid-fluid interfaces of the immersed structure are modified by the coupling of the fluid dynamics laws with the mechanical laws of the solid involved in the process. For decades, this problem has been extensively studied and theories have been developed that can simulate the complexity of this phenomenon. One of the major difficulties was the introduction of a model that could overcome the difficulty of classical mechanics due to the increase of a singularity in partial differential equations and therefore a discontinuity in the presence of the crack. An innovative approach comes from the use of peridynamics, a theory of the solid continuous that allows to study of the interaction of the two phases involved and allows the study of the formation and propagation of cracks. This manuscript is devoted the study of the preliminary stage of the erosion of an ablative porous solid by a method based on peridynamics and the incomprehensible three-dimensional formulation of the Navier-Stokes equations, using a technique called the *Immersed Boundary Method* (IBM). Direct numerical simulations (DNS), based on this methodology, to simulate the crack of porous material fibers in laminar and stationary regime in a channel flow; the software was developed and validated by F. Dalla Barba based on CaNS (*Canonical Navier-Stokes*) open-source software developed by P. Costa. The first chapter of this thesis focuses on the analysis of the interaction phenomenon by presenting different approaches that can be used to deepen the analysis. The methodology for studying the problem is explained in a general manner, before focusing on the theory of peridynamics and moving on to numerical methods used for simulation. In the end, the software used in the formulations is presented to provide a presentation and analysis of the results and their conclusions, and possible future developments in the engineering field. It has been noticed that the fibers of the material break due to the fluid dynamic forces generated by the fluid phase. Material damage is not an instantaneous phenomenon, but rather a continuous process that causes the solid to continuously decay and fracture.

Contents

CHAPTER 1

Introduction

Fluid–structure interaction (FSI) is a class of problems with mutual dependence between fluid and structural mechanics. It is a multi-physical phenomenon, that is, it takes into account different physical phenomena, which involves the interaction between a flow that causes the deformation of a solid structure and/or vice versa, in which the laws of fluid dynamics and structural mechanics are implicated. The flow behavior is influenced by the shape of the structure and its motion, and the fluid mechanics forces acting on the structure influence its motion and deformation. Interactions of this type can affect different physical phenomena in different fields of engineering. In the field of bio-medical and bio-mechanical engineering, for example, it may be necessary to study the pumping of blood from the ventricles of the human heart, accompanied by the opening and closing of heart valves and blood flow and arterial dynamics in brain aneurysms. In the sphere of mechanical and civil engineering of relative importance is to study a building in response to the stresses of the wind. In aerospace, aeronautics and mechanics, the issue of fluid-structure interaction is evident in the fluttering of aircraft wings, the flapping of airport winds, the deflection of wind turbine blades, the inflation of car airbags, or in the dynamics of spacecraft parachutes [1]. The FSI problem is strongly non-linear and time-dependent due to the coupling between the governing equations of solid mechanics and flow equations. The challenges involved in FSI can be categorized into three areas: problem formulation, numerical discretization, and fluid–structure coupling. The problem formulation takes place at the continuous level, before the discretization. It is important to remember that the modeling choices made at the continuous level have an effect on the numerical discretization that are most appropriate for the case at hand. The domain could be in a state of motion or not. It is necessary to simultaneously satisfy the sets of equations and boundary conditions associ-

ated with the fluid and structure domains. The domains do not overlap and the two systems are coupled to the fluid-structure interface, which requires a set of physically significant interface conditions. These coupling conditions are the compatibility of kinematics and stresses to the fluid-structure interface. The domain of the structure is usually in motion and its movement follows the material particles, or points, that constitute the structure. Analytical solution of this type of problem is very challenging due to the above-mentioned aspects. Despite this, computational FSI research has made significant progress, particularly in recent decades, with both core FSI methods that form a general framework and specific FSI methods that target specific classes of problems. Various computational methods have been utilized to solve equations governing fluid dynamics (most commonly the Navier-Stokes equations) and structure dynamics. The coupling between them has been examined after unfortunate events such as the collapse of the Tacoma Narrows bridge, vibration of deep water risers in oil rigs etc. [21]. The major classification of numerical methods is based on the way in which fluid and solid coupling is introduced, the generation of grids (whether they change with the fluid/solid domain), and the discretization process to solve the final algebraic equations [21]. A classification is based on the numerical approach used, and therefore on the mathematical framework designed to solve for fluid and solid domains. The FSI problems can be broadly divided into two approaches: the monolithic approach and the partitioned approach. In the case of a monolithic approach, unified mathematical governing equations are defined for both fluid and solid, and the entire domain is solved as one entity. In a different way, the partitioned method treats the fluid and the structure as two different computational fields, with the respective governing equations in their domain, mesh and numerical algorithm. Interface conditions are explicitly used to communicate information between fluid and structural solutions [14] [21]. As mentioned above, there are many classifications for FSI problems. Another example of classification of FSI solution procedures is based on the treatment of meshes: conforming mesh methods and non-conforming mesh methods. The nature of the coupling, and the types of interaction, is exclusively determined by the two systems under consideration. Of fundamental importance is the knowledge and the forecast of the instability phenomena that can arise within the system limiting the range of functionalities of the entire system. In most cases, simulations are implemented by simplifying the modeling of one of the two mediums or by using specific coupling procedures to permit fluid computational codes on one side and solid on the other, to task concurrently. The complexity of the FSI problem increases when the mechanical fracture of the solid due to the action

of hydrodynamic forces (hydraulic fracture) [8, 6] is taken into account. In several occasions of practical interest, it is essential not only to predict the stress conditions under which the structure will undergo failure, but also to determine its modes of failure and how the level of local damage impacts the resistance of the entire structure. In the aerospace industry, this class of investigation is necessary for the prevision of the propagation and initialization of the crack on the skin, on the spars, or on the ribs of aircraft wings due to the stress of fatigue caused by aerodynamic forces acting on them. The research of fracture phenomena is a multi-disciplinary study, in the geotechnical field, for example, is used for the study of the fracking process, a technique to extract gas and oil from shale rocks, as well as erosion processes due to the water or the wind. The complexity of the study of hydraulic fracture is mainly due to two problems. The first is based on the low reliability of local theories of solid mechanics in predicting structure behavior when account is taken of crack formation. The latest is due to the generation of new solid-fluid interfaces, from solid-solid contact regions and the effect of lubrication forces [6]. One of the major challenges in predicting fracture formation depends on the fact that the origin of the crack changes the state of deformation and stress of the structure at the micro-structural level, making elastic linear analysis completely ineffective to predict failure. Even if the total gross load of a material does not exceed its ultimate strength, cracks can still propagate catastrophically. In addition, local continuous theories are not reliable for prediction and crack propagation. In fact, such theories are based on mathematical models that use partial differential equations, therefore, in the presence of a crack, singularities arise that are difficult to manage. In addition, as anticipated before, by the formation of a crack induced by the fluid and solid interaction, new interfaces arise that evolve over time that must be considered, as well as the exchange of momentum, mass and energy through them. Archival literature reports different attempts to numerically address the problem. Among them, a popular and innovative numerical technique for applications consists in the usage of phase fields methods [34, 4], e.g. the so-called *Enriched (Extended) Finite Element Method* (XFEM), coupled with simplified models for the fluid to account for hydraulic stresses and lubrication forces [6, 4]. These methods are utilized for fracture-related problems, in contrast to the classical finite element method (FEM), specific functions are utilized at the point where discontinuity occurs without re-meshing at each iteration [34, 37]. The *Distinct Elements Method* (DEM) [12, 15, 38] has been developed as an alternative to this approach. These models, in the same manner of the XFEM, are also coupled with models capable of computing the forces and stresses exercised by

the fluid. Despite their accuracy and reliability for specific applications, most approaches lack generality and are restricted to very limited cases and poorly characterized local fluid dynamics. In this thesis, a software based on a numerical method is used to simulate three-dimensional FSI problems with fluids that induce fractures in the solid, where the physics of the fluid are entirely resolved. In particular, the goal is to simulate and analyze the fracture of a porous material in a channel flow, for ablative materials. In this context, we aim to solve the problem in a framework based on a coupling of the incompressible equations of Navier-Stokes with peridynamics through an immersed boundary technique. Peridynamics is used to address solid and fracture mechanics. The theory of peridynamics consists of a reformulation of a continuum mechanisms, developed by Silling [26], relying on integral equations. In recent years, peridynamics has been successful in solving problems related to fluid flow, solid-fluid interactions, fractures, and erosion. In this model, the solid is represented by a set of points, material Lagrangians particles that interact with each other through a short-range potential. The mechanics on which the model is based, consider intrinsically the deformation of the solid, that is simply described by directly solving momentum-balance integral equation governing the dynamics of the particles. The material points mutually interact via micro-potentials; the latter give rise to mutual internal forces that act over a finite spatial distance referred to as *horizon*, δ. The main advantage of peridynamics is its ability to describe intrinsically and effectively manage the crack formation and branching. In this framework solid mechanics is formulated in terms of an integral balance of linear momentum. Indeed, when a fracture is taken into consideration peridynamics removes the instabilities due to the singularity of the partial differential equations caused by the formation and propagation of cracks, using integral equations. The methodology described in this manuscript is based on the so-called bond-based [30] peridynamics model and uses constitutive relations for linear-elastic solid with brittle mechanical properties. The immersed boundary method (IBM) is used to establish the coupling between the solid and liquid phases. By using this technique, fluid dynamics equations can be solved in a computational structured and fixed grid that does not conform with the solid-fluid interface. The boundary conditions of no-slip and no-penetration at the border between solid and fluid, are imposed to the fluid using fictitious forces that reproduce the presence of the solid material. The flow is forced to move at the same velocity as the solid material near the solid surface and the relative velocity between the two phases is automatically respected by setting to zero the relative velocity between them. The benefit of this technique is the use of a fixed Eulerian grid does not require-

ment to be recalculated at every time step during the simulation, reducing the computational cost. Furthermore, modeling the forcing makes the method effective and accurate in specifying wall conditions for complex geometries, which turns these schemes suitable for several cases. In this IBM framework, the *normal probe method* [10, 36, 32] is employed to determine the forces and tensions generated by the interaction and deformation of the fluid with the solid surface. The code to simulate the fluid phase is based on the open-source software CaNS [5], developed by P. Costa, while the solid phase solver was developed from scratch by F. Dalla Barba in both the bond-based formulation and in the state-based formulation on peridynamic theory. The use of explicit techniques is used in all resolution schemes in a parallel computing structure through Message-Passing Interface (MPI), which is one of the most common and famous computer communication protocols. The software has been utilized in this specific study case to develop a numerical simulation of the failure of solid fibers of a porous material immersed in a fluid domain characterized by a laminar regime with low Reynolds number. The main aim is to study how these fibers of material behave mechanically over time and consequently in terms of displacements, stresses and strains with particular regard to the fracture problem for which the nature of the fracture is being investigated, or whether it is caused by a peak of forces/stresses that develop as a result of motion or by fatigue, without the need to reach certain conditions such as yield strength. In this case, the study is aimed at identifying the behavior of ablative materials. The study of the phenomenon in fact can be of considerable interest in many spheres not only engineering, in fact it is possible to simulate scenarios that include damage and fracture in natural or artificial porous materials such as bone, wood, rock and sandstone.

CHAPTER 2

Methodology

This chapter provides a detailed description of the numerical modeling used for the simulations, a three-dimensional fluid-structure interaction problem involving fracturing. A brief overview of peridynamic, immersed boundary method (IBM), and Navier-Stokes equations are reported.

2.1 Theoretical modeling of solid mechanics and its numerical method

The aim of this section is to present an overview of the most recent methods for numerical modeling of solids. In particular, the focus is on modeling the mechanical fracture and its numerical techniques used for FSI problems.

2.1.1 The continuum mechanics: Local and non-local theories

Classic continuum mechanics is the most practical theory used to describe solid mechanics, including linear and more complex elastic behavior such as non-linear and plastic behavior. In the last decades, different formulations have been found and can be organized into two different categories: Local and non-local theories. The local theories are based on the idea that the material is a continuum, and it is composed of a dense set of idealized-infinitesimal material particles, each of which is a mass point that only exchanges mass, momentum, and energy with its closest neighbor particles [25]. Each point has material characteristics and the inner interaction between two close points is a contact force that acts through zero distances [29]. The result, in the local model, is the stress plate at a particular point determined exclusively by the

strain at that point only. This model is based on the mathematical description of partial differential equations (PDEs) [29] [19]. However, we must consider the fact that in the material coexists forces acting at different length scales, for example, the long-range forces between non-neighboring particles, which can have an important role in the macro structural behavior of the material. Furthermore, the real material is composed of a complex structure that exhibits interactions at the nano-and micro-scales that classical mechanics fails to observe, particularly the ones that require breaking down the material into multiple scales. In these terms, the continuum local description is not longer reliable, the real material structure shows behaviors over different length-scales making the study of the behavior of the material through classical mechanics not very effective and strongly dependent on the size grid as well as on the characteristic length-scale [29] [25]. Similar considerations can be made when a discontinuity, such as a crack, occurs. Partial differential equations, in these terms, present singularly along discontinuities that make the theory of local treatment very complex. Non-local theories provide a general view into the continuum solid, and the hypothesis of the continuity at any arbitrary length-scale can be relaxed. These theories are based on the concept that the state of the point is influenced not only by the deformation of the point itself but also by the points located in a finite volume around the considered one, introducing a mutual connection between points across a finite region. During this term, whenever the radius becomes infinitely large the non-local theory becomes the continuous version of the molecular dynamics model, establishing the connection between the classical continuum mechanics (local) and molecular dynamics [19]. One of the most important aspects introduced by the non-local theory is the capability of studying, not only the effects on the macro scales but also the results of the microstructure of the material at molecular and atomic scales. A distinction can be made between integral-type and gradient-type non-local models [19] [29]. The first one, the integral-type model, is based on a constitutive law that connects the forces at the material point to some weighted average of the deformation of other points. The second model, the gradient-type, uses higher-order derivatives to describe the deformation and strain fields in the proximity of the material point. The non-local theories still assume the media as a continuum, and both divisions introduce a characteristic length that can be related in the same range of grain size, pore size, or crack and micro-crack. The theory of non-local is capable not only of describing macro-scale affects but also the effects of molecular and atomic scales, a phenomenon that has been found to be extremely challenging to perform with local theories. Its growth is not only determined by local

stress or deformation but also depends on the deformation that takes place in a certain vicinity of the micro-crack. Despite the advantages of non-local theories, they still have certain limitations. Spatial derivatives remain included in their mathematical formulation, so such models, similar to local theories, break down in the presence of discontinuity, leading to the problem of singularity, as in the case of crack.More recently, Silling (2000) [26] proposed a non-local theory that requires no spatial derivatives: peridynamics theory (PD). In short, the theory of peridynamic is a re-modelling of the equation solid mechanics motion, replacing spatial derivatives with integral spatial equations, that are more suited for discontinuities, avoiding the problem of singularities. The material damage is taken into account in the constitutive laws of peridynamics. It permits the modeling of fracture initialization and propagation, without a special grow crack treatment [19].

2.1.2 Numerical methods for modeling discontinuities solid media

Cracks, porosity, and imperfections are easily found in materials, and control most of the physical and mechanical behavior of materials. The micro-crack, therefore the failure of the material, develops when the release of stress in situ is concentrated at the tip of discontinuities and micro-cracks happen when they overcome the body resistance [14]. The need to study, model, and resolve inhomogeneities has led to the development of several numerical methods for the study of solid mechanics. In fracture mechanics, numerical methods are divided into discrete, continuum, and hybrid methods [22]. The choice of the use of continuum or discrete methods depends on the size, scale, and discontinuities, concerning the size or scale of the problem [2]. Among all the continuum methods, the Extended Finite Element Method (X-FEM), derived from the Standard Finite Element Method (FEM), has gained much attraction in fracture mechanics. The classic Finite Element Method divides a large system into smaller elements, discretizing continuum space, that intersects at nodes, and solving spatial differential equations on it. The solution, the displacement at any point within the element, can be calculated through appropriately chosen interpolation functions, from the displacement at every node [2]. However, when the crack takes place crack prediction procedures, for FE models, use advanced element formulations and a re-mesh is necessary in the near region of the crack path, holes, or inhomogeneities [34] [38]. With the standard finite element method, cracks are considered to be inner boundary surfaces that are explicitly meshed. X-FEM, the advanced method, allowed the modeling

of internal (or external) boundaries, such as holes, inclusions or cracks without re-meshing the geometry. It also permits strong discontinuities (discrete cracks) to arbitrarily cut through elements [33] [37]. The idea behind X-FEM is adding to the standard polynomial shape functions used in the finite element model, some others functions to model the discontinuities, in order to improve the accuracy of the stress intensity factors, in some problems where some aspect of the solution field is known a priori [34]. In particular, the modeling of the crack is given using two additional tow sets of nodal shape functions. The first set includes a discontinued generalized function(Heaviside function) which describes the crack path and is used to represent the crack opening displacement. On the other hand, the second set is asyntomatic functions defined at the crack-tip origin [34] [33] [37]. The most significant advantage of the X-FEM model is that allows of the description of discontinuities and their development without requiring the definition of a new mesh at each iteration. The model, although accurate, does not consider the crack intrinsically, which is the main characteristic of peridynamic. On the other hand, returning to the distinction previously made, the discontinuum methods most used are DEM, DDA, and BPM. Concentrate on the DEM (distinct element method) approach, which is one of the most recent methods for simulating the fracture process [2] [38]. This approach is used to simulate large movements in blocky rock masses and then used for soils that were modeled as assemblies of disks [2]. The DEM is a Lagrangian method where the medium is partitioned into discrete elements, that interact via contact forces. In particular, it is assumed that the solid is split by discontinuities that determine a set of finite-size polyhedral or spherical blocks [2]. The forces acting at the block edges arise from their interactions with the enclosed blocks and the displacement is calculated by Newton's second law of motion [2]. This method uses an explicit central finite difference method, in a time domain, to solve displacements and the velocities. Contact forces are described by adequate contact laws to constitute the mechanical behaviors between block faces, such as elastic laws coupled with Coulomb friction, attractive forces, also Van Der Waals forces can be implemented [2] [15] [12]. Nevertheless a priori knowledge of the block shape of the block is required, which influences the overall response of the system. The formation of discontinuity is not possible through the block but only between them (by the implementation of cohesive force patterns), the cracks, therefore, must propagate in the block-block contact region, between the faces of the elements.

2.2 Methodologies of Study of the FSI

The fluid-structure interaction (FSI) class involves problems that are mutually dependent on both the fluid dynamics and structural mechanics parts. Challenges related to computational FSI can be classified into three categories: problem formulation, digital discretization, and fluid-structural coupling [1]. Two approaches can be broadly classified as the numerical methods used to solve these FSI problems: the *monolithic approach* and the *partitioned approach* [14]. The monolithic approach pairs the fluid and structure dynamics in the same framework to form a single equation for the whole problem, which is solved in parallel by a unified algorithm. The interface conditions are implicitly described within the equation. This approach is usable for a multi-disciplinary problem, reaching a better accuracy, but requires more resources to maintain a specialized code. In contrast, the partitioned criterion studies the fluid and the structure separately with their respective mesh discretization and numerical algorithm, making explicit the conditions at the interface to communicate information between the fluid and the structure. Sophisticated results can be obtained, between fluid and structure. The challenge of this method is to coordinate the two algorithms to achieve accurate fluid-structure iteration since the position of the interface that divides the fluid and the structure domains is not known a priori and usually changes over time. Therefore, the partitioned method requires the detection of the new interface position and its quantities. A further general classification of solution procedures is based on mesh treatment: *conforming mesh method* and *non-conforming mesh methods*. The first one treats the conditions interface as part of the solution, as physical conditions, requiring a mesh to conform to the interface. Due to the movement and/or deformation of the solid structure, an update of the mesh is needed. One popular FSI method in this class is the Arbitrary Lagrangian-Eulerian (ALE) technique which incorporates the moving mesh explicitly into the fluid dynamics equation. On the other hand, the non-conforming mesh methods, impose on the model equation constraints, such as the boundary location and the related interface conditions, consequently, non-conforming meshes can be employed a mesh update is avoided. This methods category is based on the framework of the immersed methods (IBM), which adds terms to the fluid equations (e.g. force-equivalent terms) to describe the fluid-structure interaction [22].

2.2.1 ALE: Arbitrary Lagrangian-Eulerian method

The ALE technique is premised on the discrimination of the field by using conform computational meshes, which an unstructured, to solve Navier-Stokes equations. This method includes both pure Lagrangian and pure Eulerian formulations [31]. The mesh nodes can move with the material -Lagrangian method- the track of the surface and the boundary conditions are easy to define. The mesh can be fixed -Eulerian method- while the material passes through it, or the nodes can be moved in any other prescribed way [13] [31]. The solution of the governing equations evolves in time, using discrete time steps, and the governing equations of the fluid phase are solved via the finite-volume method. There are two approaches to implementing the ALE equations. The first way performs the couple equations for computational fluid mechanics but can handle only a single material in the element. In the alternative approach, the time step is divided into two phases. The solution begins with a Lagrangian phase, where the mesh nodes move with the material, and the equilibrium equations (velocity changes and internal energy) are calculated. In addition, the second phase, the advection phase, adjusts transport mass, internal energy, and momentum across the cell boundaries, this resembles moving the mesh vertices (remapping) to their Lagrangian position [31]. A set of boundary conditions, such as no-slip and no-penetration, are imposed on the mesh nodes located on the surface, along these nodes the structure and the vertices fluid have the same normal velocity. Although the disadvantage of the continuous re-meshing and updating the mesh to preserve conformity to the moving fluid-structure and the calculation of convective fluxes of all the fluid-dynamic fields lead to a large computational cost of this simulation, the primary advantage of the ALE technique relies on the accurate treatment of the interfaces.

2.2.2 IBM: Immersed Boundary Method

The IBM belongs to the class of the non-conforming method, the need of re-meshing is completely removed and the Navier-Stokes equations are solved on a fixed-Eulerian-grid and structure grid [18], which does not conform to the immersed solid surface. The term "immersed boundary method" was initially used to refer to a technique created by Peskin [18] [20] [14] to simulate cardiac mechanics and blood flow [20]. The imposition of boundary conditions to the IB is the key factor in the development of an IB algorithm, which is also what distinguishes one IB method from another. In general, BCs are not applied directly on the nodes of the grid located on the wall (i.e. by setting up=0), but

they are performed by introducing a source of friction force, which is applied to the flow in proximity of the interface. In this way, the flow is locally forced to move with the same local velocity of solid walls. If the relative velocity between the flow and the solid is zero, no-slip and, no-penetration, BCs are indirectly satisfied. The IB methods can be typically categorized into two categories: *continuous forcing approach* and *discrete forcing approach* [20] [18], depending on the mode the boundary conditions are enforced on the interface. In the primary approach, the forcing term is implemented at the continuous equations, Navier-Skoes equations, before the discretization. The issue with this method is the definition of the continuous forcing function needed to enforce the correct boundary conditions [18]. Instead, in the discrete forcing approach, the forcing term is inserted after the discretization of the fluid phase, to take into account the presence of the solid [20]. An attractive feature of the continuous forcing approach is that it is formulated independently of the underlying spatial discretization. On the other hand, the discrete forcing approach is very dependent on the discretization method.In addition, the first mode is adapted to the deformable solid, while it manifests, in general, singularities for rigid bodies, on the terms of forced friction. In contrast, the second approaches, have been shown to be successfully employed both for rigid and deformable solid. Various approaches to the IB method have been employed over the years for implementing FSI problems. One of the biggest advantages that IBM brings is that the mesh does not have to conform/adapt to the moving/deforming immersed body. This contributes to eliminating the complexity and the computationally expensive procedure of Eulerian re-meshing to every time step. The continuous IB method originally conceived by Peskin [10] [20] [35] for flows around flexible membranes is based on the idea of determining a force, in a Lagrangian position, to apply to the flow equations (via Direct Delta faction) in the fixed reference frame. The force term used is simply a result of the membrane's deformation and its elastic properties. However, one of the biggest problems of Periskin's method is the numerical stability due to the stiffness introduced into the problem with the elastic feature of the immersed body. The method can lead to hydrodynamic forces that are potential sources of instability [10]. Since the introduction of this method, several modifications have been proposed. Uhlmann [32] [35] [36] [10] first developed an efficient discrete forcing IBM for the moving particle flow using a direct forcing approach in a finite-volume and pressure-correction frame. The base idea was to introduce a fictitious domain method that did not use a feedback mechanism to obtain the forcing term [35]. This method presents fewer oscillatory particle forces than existing direct methods, due to the combination of the capacity of

the IB method to smoothly transfer quantities between the two grids and, on the other hand, the effectiveness of an explicit and direct formulation of fluid-particle interaction force. In this implementation, the Navier-Stokes equations of particulate flows are solved on a Cartesian grid, referred as to the Eulerian grid, whereas the forcing term is computed in a uniform distribution of Lagrangian markers (on the immersed body) and transferred to the Eulerian grid via transfer kernels [36]. In this way, the no-slip and no-penetration conditions are imposed on the fluid proximate to the interface with the immersed solid. The forcing function is calculated by interpolating the velocity fields of the Lagrangian point fluids, the computation of the Lagrangian representation of the forcing, and the spreading of the latter on the Eulerian grid. Uhlmann introduced a direct-forcing IB method that utilizes the high-order regularized Delta function in the velocity interpolation and the force distribution. In this frame, various approaches have been developed based on Uhlamann's idea, utilizing different interpolation kernels and procedures [32] [10] [36]. This class of methods, referred to as *multi-direct forcing* [35] IBM, is currently the state-of-the-art for FSI problems with moving boundaries. The computation of the back-reaction exerted by the fluid on the solid is the main issue with multi-direct forcing schemes. In this present work, the method of multi-direct forcing is used to impose the boundary conditions on the wall to the fluid-solid interfaces, whereas the calculation of hydrodynamic forces is left to the *normal-probe* method [36].

2.3 Theory of peridynamic

2.3.1 Basics of Peridynamic Theory

The term "peridynamic" first appeared in Silling (2000) [26] and comes from the Greek roots for near and force [29]. This method falls into nonlocal theories because particles, separated by a finite range, can interact with each other. The maximum distance across which points interact through a *pairwise force* is called the *horizon*. Those are internal forces of a continuous solid considered as a system of pair interactions equivalent to springs. The scale of the horizon is strongly dependent on the nature of the solid and the interactions turn more local with a decreasing horizon, capable of bridging the nano to macro length scale. The classical techniques based on the spatial derivatives fail when we attempt to study a more severe discontinuity, such as a crack. Since the weak solution when the phase changes and the need to redefine the body when the

crack occurs, to align the crack to the boundary, requires knowing a priori where the discontinuity is located. The limits of these methods are overcome with the integration technique, where there is no discernment between points on the body where discontinuities or any of their spatial deviates take place. Thus allowing the spontaneous formation of discontinuity without the need to know its position in advance. In its original wording, termed a *bond-state peridynamic model* (BPD), the points interact via pairwise forces with neighboring material points. The interaction between two material points depends only on their deformations. This first theory suffers from significant restriction, in particular the Poisson ratio is always 1/4 for isotropic materials. Later, Silling et al. (2007) [29] [30] generalized the BPD model introducing the concept of state. The outcome concept preserved the idea of bonds carrying the forces between two points, the bond force is not determined only by their deformation state but it depends on the deformations state of all the bonds within the horizon of each point (figure 2.1). The resulting theory is called the *state-bond peridynamic model*, and it overcomes the problems of the previous, bond-based, theory. It can describe the behavior of any isotropic solid material model in which any Poisson ratio can be prescribed.

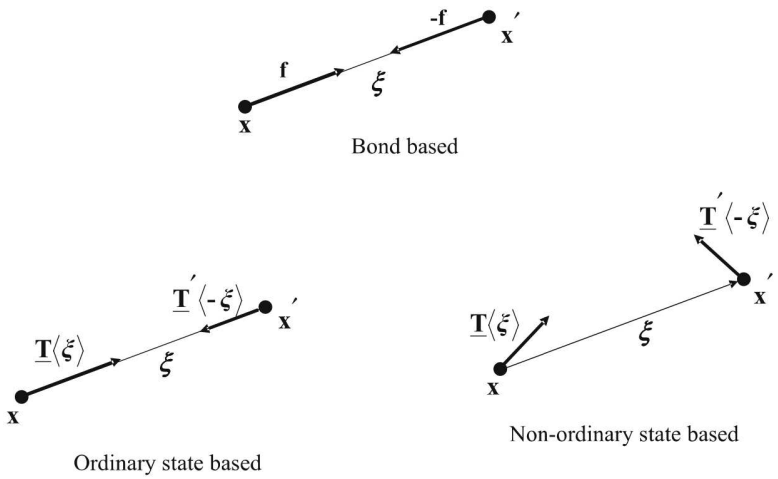

Figure 2.1: Representation of the different formulations of the peridynamic theory.

2.3.2 The governing equations of peridynamic

The fundamental equation of peridynamic relies on a Lagrangian formulation of the conservation of linear momentum in continuum media. In this framework,

a solid, closed, and bounded body, denoted as $\mathcal{B}$, is represented as a set of finite-size material nodes. The points that interact via micro-potential, give rise to a mutual internal force that acts across the finite spatial distance, *horizon* δ. Each node communicates with a set of other points referred to as the *neighborhood* $\mathcal{H}_{\mathrm{X}_0}$:

$$\mathcal{H}_{X_0} = \{\boldsymbol{X}_0^{'} \in \mathcal{B}, ||\boldsymbol{X}_0^{'} - \boldsymbol{X}_0|| < \delta\}, \tag{2.1}$$

where $\boldsymbol{X}_0^{'}$ and $\boldsymbol{X}_0$ are the Lagrangian spatial coordinates of the two pair nodes, undeformed and unloaded, in reference configuration of the body. $\boldsymbol{X}_0^{'}$ is centered in $\boldsymbol{X}_0$ and contains the position vectors of the material. Hence, the motion of the Lagrangian point belonging to the body is expressed as $\boldsymbol{X}(\boldsymbol{X}_0, t)$, where $\boldsymbol{X}_0$ represents the Lagrangian coordinate of the body, in this case in a deformed condition, at time $t \geq 0$. The velocity is described by the displacement derivative, in Lagrangian terms:

$$\boldsymbol{V}(\boldsymbol{X}_0, t) = \frac{d}{dt}\boldsymbol{X}(\boldsymbol{X}_0, t). \tag{2.2}$$

Let's define $\boldsymbol{F}(\boldsymbol{X}_0, t)$ as an external force of unit volume and $\boldsymbol{L}(\boldsymbol{X}_0, t)$ as the acting unit volume force at time t on the material point $\boldsymbol{X}_0$ due to interaction with the elements in the neighborhood area. By using Newton's second law to a limited area of the body $\mathcal{P} \in \mathcal{B}$, obtains:

$$\frac{d}{dt}\int_{\mathcal{P}} \rho(\boldsymbol{X}_0)\boldsymbol{V}(\boldsymbol{X}_0, t)dV = \int_{\mathcal{P}} [\boldsymbol{L}(\boldsymbol{X}_0, t) + \boldsymbol{F}(\boldsymbol{X}_0, t)]dV \tag{2.3}$$

where $\rho(\boldsymbol{X}_0)$ stands for the density of the body. This Lagrangian equation which governs the motion of each material point $\boldsymbol{X}_0$ can be rewritten into its differential form, as:

$$\rho(\boldsymbol{X}_0)\frac{d}{dt}\mathbf{V}(\boldsymbol{X}_0, t) = \boldsymbol{L}(\boldsymbol{X}_0, t) + \boldsymbol{F}(\boldsymbol{X}_0, t) \quad \forall \boldsymbol{X}_0 \in \mathcal{B}, t \geq 0 \tag{2.4}$$

The second Newton's law re-elaborated all over the total body $\mathcal{B}$, leads to the integral expression:

$$\frac{d}{dt}\int_{\mathcal{B}} \rho(\boldsymbol{X}_0)\boldsymbol{V}(\boldsymbol{X}_0, t)dV = \int_{\mathcal{B}} \boldsymbol{F}(\boldsymbol{X}_0, t)dV \tag{2.5}$$

Note that the force $\boldsymbol{L}(\boldsymbol{X}_0, t)$ does not appear in the last equation, since it is an internal force that balances itself. This comes out by placing $\mathcal{P}$=$\mathcal{B}$ in equation

(2.3) and subtracting equation (2.5) to equation (2.3) :

$$\int_{\mathcal{B}} \boldsymbol{L}(\boldsymbol{X}_0, t) = 0, \tag{2.6}$$

which formally demonstrates that the internal force is a self-balancing force and it can be neglected within the domain. In particular, that leads to the fact that for any given force field $\boldsymbol{L}(\boldsymbol{X}_0, t)$ always exists an antisymmetric vector-valued function,

$$\boldsymbol{f}(\boldsymbol{X}_0^{'}, \boldsymbol{X}_0, t) = -\boldsymbol{f}(\boldsymbol{X}_0, \boldsymbol{X}_0^{'}, t) \qquad \forall \boldsymbol{X}_0^{'}, \boldsymbol{X}_0 \in \mathcal{B}, t \geq 0 \tag{2.7}$$

thus $\boldsymbol{L}(\boldsymbol{X}_0, t)$ can be expressed as:

$$\boldsymbol{L}(\boldsymbol{X}_0, t) = \int_{\mathcal{B}} \boldsymbol{f}(\boldsymbol{X}_0^{'}, \boldsymbol{X}_0, t) dV^{'} \qquad \forall \boldsymbol{X}_0 \in \mathcal{B}, t \geq 0, \tag{2.8}$$

In the latter equation, $\boldsymbol{X}_0^{'}$ is identified as the dummy integration variable, and $dV^{'}$ is the differential volume evaluated in position $\boldsymbol{X}_0^{'}$.
It can be demonstrated that for any function $\boldsymbol{f}(\boldsymbol{X}_0^{'}, \boldsymbol{X}_0, t)$, which is named as *dual force density* or *pairwise force density*, it can be found a function $\boldsymbol{t}(\boldsymbol{X}_0^{'}, \boldsymbol{X}_0, t)$ so that:

$$\boldsymbol{f}(\boldsymbol{X}_0^{'}, \boldsymbol{X}_0, t) = \boldsymbol{t}(\boldsymbol{X}_0^{'}, \boldsymbol{X}_0, t) - \boldsymbol{t}(\boldsymbol{X}_0, \boldsymbol{X}_0^{'}, t) \quad \forall \boldsymbol{X}_0^{'}, \boldsymbol{X}_0 \in \mathcal{B}, t \geq 0. \tag{2.9}$$

Where $\boldsymbol{t}(\boldsymbol{X}_0^{'}, \boldsymbol{X}_0, t)$ is a function denominated as *bond force density* and it represents one of the cardinal quantities peridynamics theory. By using the

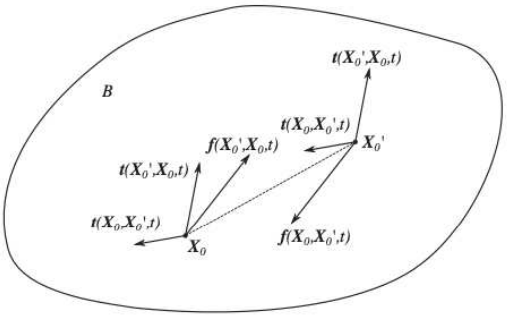

Figure 2.2: Sketch of pairwise forces acting between two material points $\boldsymbol{X}_0$ and $\boldsymbol{X}_0^{'}$,*dual force densities*, and the related *bond force densities*

last two equations (2.8) and (2.9), the equation can be reformulated as:

$$\rho(\boldsymbol{X}_0)\frac{d}{dt}\boldsymbol{V}(\boldsymbol{X}_0,t)=\int_{\mathcal{B}}\boldsymbol{f}(\boldsymbol{X}_0^{'},\boldsymbol{X}_0,t)dV^{'}+\boldsymbol{F}(\boldsymbol{X}_0,t),\quad \forall\boldsymbol{X}_0\in\mathcal{B},t\geq 0, \tag{2.10}$$

or equivalently as Silling [26]:

$$\rho(\boldsymbol{X}_0)\frac{d}{dt}\boldsymbol{V}(\boldsymbol{X}_0,t)=\int_{\mathcal{B}}[\boldsymbol{t}(\boldsymbol{X}_0^{'},\boldsymbol{X}_0,t)-\boldsymbol{t}(\boldsymbol{X}_0,\boldsymbol{X}_0^{'},t)]+\boldsymbol{F}(\boldsymbol{X}_0,t),\quad \forall\boldsymbol{X}_0\in\mathcal{B},t\geq 0. \tag{2.11}$$

In a peridynamic body, these two expressions (2.10) and (2.11) represent the balance of the linear moment. To solve the problem, it is required to introduce a constitutive model to compute the forces (bond force density or pairwise force density) according to the macroscopic properties of the material and the state of deformation of the body. The constitutive relations are derived by introducing the concept of peridynamics state (introduced at the beginning of this paragraph), where the $\boldsymbol{X}_0$ point interacts with the other nodes within a region of adjacent space. From equation (2.1), the *family* of $\boldsymbol{X}_0$ is defined as follows:

$$\mathcal{H}=\{\xi\in(\mathbb{R}^3-(0)),(\xi+\boldsymbol{X}_0)\in(\mathcal{H}_{X_0}\cap\mathcal{B})\}, \tag{2.12}$$

where $\xi\in\mathcal{H}$ is a vector that indicates the *bond* connected to $\boldsymbol{X}_0$, and it is centered at $\mathbf{0}$ and contains a bond. The bond ξ can be defined by the formulation:

$$\xi=\boldsymbol{X}_0^{'}-\boldsymbol{X}_0,\quad \forall\boldsymbol{X}_0\in\mathcal{B},\boldsymbol{X}_0^{'}\in\mathcal{H}_{X_0}, \tag{2.13}$$

whereas in a deformed state, the bond is defined as:

$$\zeta=\boldsymbol{X}^{'}(\boldsymbol{X}_0^{'},t)-\boldsymbol{X}(\boldsymbol{X}_0,t)\quad \forall\boldsymbol{X}_0\in\mathcal{B},\boldsymbol{X}_0^{'}\in\mathcal{H}_{X_0},t\geq 0, \tag{2.14}$$

with η the *bond displacement vector* :

$$\eta=\zeta-\xi \tag{2.15}$$

Let's define a *peridynamic state* of order m, $\underline{\boldsymbol{A}}(\boldsymbol{X}_0,t)\langle\xi\rangle:\mathcal{H}\longmapsto\mathcal{L}_m$, where $\mathcal{L}_m$ denotes the set of all tensors of order m, as:

$$\int_{\mathcal{H}}\underline{\boldsymbol{A}}(\boldsymbol{X}_0,t)\langle\xi\rangle dV_\xi=\int_{\mathcal{H}_{X_0}}\underline{\boldsymbol{A}}(\boldsymbol{X}_0,t)\langle\boldsymbol{X}_0^{'}-\boldsymbol{X}_0\rangle dV^{'} \tag{2.16}$$

The peridynamic state $\underline{\boldsymbol{A}}(\boldsymbol{X}_0,t)$, is defined as a function on $\mathcal{H}$ that maps the bonds $\xi\in\mathcal{H}$ into a tensor of order m, including vectorial and scalar quantities; it is worth to remaking that the state depends on the Lagrangian position $\boldsymbol{X}_0$

and time, t. Thereby, plying the notion of peridynamic state, it is possible to determine the bond force density as follows:

$$\boldsymbol{t}(\boldsymbol{X}_0^{'}, \boldsymbol{X}_0, t) = \underline{\boldsymbol{T}}(\boldsymbol{X}_0, t)\langle\xi\rangle = \underline{\boldsymbol{T}}(\boldsymbol{X}_0, t)\langle\boldsymbol{X}_0^{'} - \boldsymbol{X}_0\rangle, \tag{2.17}$$

where, $\underline{\boldsymbol{T}}(\boldsymbol{X}_0, t)\langle\xi\rangle$ is the *force vector state* [30]. To sum up, in the light of the equation (2.11) and the definition of Lagrangian velocity brought up in equation (2.2), the equations governing the peridynamics theory are:

$$\boldsymbol{V}(\boldsymbol{X}_0, t) = \frac{d}{dt}\boldsymbol{X}(\boldsymbol{X}_0, t), \tag{2.18}$$

$$\rho(\boldsymbol{X}_0)\frac{d^2}{dt^2}\mathbf{X}(\boldsymbol{X}_0, t) = \boldsymbol{L}(\boldsymbol{X}_0, t) + \boldsymbol{F}(\boldsymbol{X}_0, t), \tag{2.19}$$

$$\boldsymbol{L}(\boldsymbol{X}_0, t) = \int_{\mathcal{H}_{X_0}} [\underline{\boldsymbol{T}}(\boldsymbol{X}_0, t)\langle\boldsymbol{X}_0^{'} - \boldsymbol{X}_0\rangle - \underline{\boldsymbol{T}}(\boldsymbol{X}_0, t)\langle\boldsymbol{X}_0 - \boldsymbol{X}_0^{'}\rangle]dV^{'}. \tag{2.20}$$

Certainly, the constitutive relations depend on the nature of the material. In other words, they are laws describing the behavior of a material, in terms of the deformation of the body and possibly other variables. As discussed in the opening of this chapter, it is possible to differentiate three different models of peridynamics that can be identified based on the constitutive model used [26] [30]:

- *bond-based peridynamic* is the original formulation elaborated by Selling [4]. In this pattern, in the deformed configuration of the body ζ, the pair bond force density vectors are parallel to their relative position vectors and equal in magnitude.

- *ordinary state-based peridynamic*, the vectors are still parallel to their relative position vectors but can be diverse in magnitude.

- *non-ordinary state-based peridynamic*, the vectors can be non-parallel to the related relative position vectors and different magnitudes.

In *state-based* formulations, the bond force density vectors that join two nodes also depend on all the other bonds that these two points have established with other material points within the surroundings. This script focuses mainly on the bond-based peridynamic model, used also for the analyses performed, since all applications and models reported have been elaborated on this scheme. It is important to mark, that integral equation (2.20) provides the description for the internal force balance needed to solve the ordinary differential equation

(2.19). For more details about peridynamic theory and its models, it is possible consult the Silling [19] [26] [28] [29] [30] articles included in the bibliography.

2.3.3 Bond-based peridynamic approach

The bond-based peridynamic has been introduced by Silling (2000)[26]. This theory is a special case of the more general theory, mentioned in the paragraph above, that is state-based peridynamic [26], which is able to describe a larger class of materials with concerning to bond-based model. The basis of bond-based modeling is the assumption that the bond force density associated with a bond ξ depends only on the considerate bond, and it is distinct from the others. The main advantage introduced by peridynamic consists of its capability of simply managing the discontinuities arising in a solid medium when the crack formation and branching are taken into consideration. Let's consider the next constitutive relation for the force vector state:

$$\underline{\boldsymbol{T}}(\boldsymbol{X}_0, t)\langle\xi\rangle = \frac{1}{2}\boldsymbol{f}(\boldsymbol{X}_0^{'}, \boldsymbol{X}_0, t) \tag{2.21}$$

the bond force densities will be [19]:

$$\boldsymbol{t}(\boldsymbol{X}_0^{'}, \boldsymbol{X}_0, t) = \frac{1}{2}\boldsymbol{f}(\boldsymbol{X}_0^{'}, \boldsymbol{X}_0, t) \tag{2.22}$$

$$\boldsymbol{t}(\boldsymbol{X}_0, \boldsymbol{X}_0^{'}, t) = \frac{1}{2}\boldsymbol{f}(\boldsymbol{X}_0, \boldsymbol{X}_0^{'}, t) = -\frac{1}{2}\boldsymbol{f}(\boldsymbol{X}_0^{'}, \boldsymbol{X}_0, t) \tag{2.23}$$

As mentioned above, bond-state pridynamics is not based on the idea of the state. That is, the pairwise force density depends only on the bond between two points $\boldsymbol{X}_0$ and $\boldsymbol{X}_0^{'}$, hence it can be written as [26] [11] [16]:

$$\boldsymbol{f}(\boldsymbol{X}_0^{'}, \boldsymbol{X}_0, t) = \boldsymbol{f}(\xi, \eta) = c_0\, s(\xi, \eta)\frac{\eta + \xi}{||\eta + \xi||}\lambda(\xi, t), \tag{2.24}$$

where $s(\xi, \eta)$ and c_0 are two bond parameters, respectively called *bond stretch* and *bond micromodulus* [16] [9]. The first parameter can be expressed as:

$$s(\xi, \eta) = \frac{||\xi + \eta|| - ||\xi||}{||\xi||} \tag{2.25}$$

The c_0 parameter depends on the macroscopic mechanical properties of the material, besides on the geometry and loading conditions of the specific problem. In specific, the latter can be related, in fact, to Young's modulus, E, and

the peridynamic horizon, δ

$$c_0 = \begin{cases} \frac{9E}{\pi p \delta^3}, & \text{in 2D plane-stress conditions,} \\ \frac{48E}{5\pi p \delta^3}, & \text{in 2D plane-strain conditions,} \\ \frac{12E}{\pi \delta^4}, & \text{in 3D,} \end{cases} \tag{2.26}$$

where p refers to the depth of the body along the out-of-plane direction in the two-dimensional cases. It is worth mentioning that one of the limitations concerning the bond-based peridynamic model is the Poisson's ratio ν_s. As mentioned above, in fact, the Poisson's ratio for this model is considered constant, with a fixed value of 1/4 for the three-dimensional case and the plane strain case and 1/3 for plane stress case, therefore it does not appear in the equation (2.26).

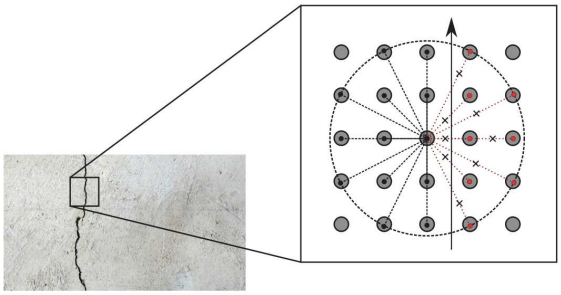

Figure 2.3: Schematic representation of crack in the theory of peridynamics. The broken bonds are indicated by the cross above them.

The main advantage introduced by peridynamics consists of its capability of simply managing the discontinuities arising in a solid medium when the crack formation and branching are taken into consideration. In the peridynamics framework, the damage is incorporated at the bond level, and the crack occurs due to the rupture of bonds when the stretch of the bond overcomes a threshold value, s_0, referred to as *limit bond stretch*. The latter can be related to the critical fracture energy release rate of the material, G_0, Young's modulus E, the horizon δ, and the geometrical configuration of the problem [27, 16]. Thus, s the bond stretch, is positive when the bond is in tension, and after the bond failure there is not no tensile force sustainable in the bond; its contribution to the internal force balance is neglected. Once the breakage of a bond takes place, the failure is persistent and there is no provision for "healing" of a failed bond; this makes the model history dependent. In this frame, a scalar-valued function has been introduced by the peridynamic model to take into account

the pairwise interaction in a bond:

$$\lambda(\xi, t) = \begin{cases} 1, & s \leq s_0, \quad \forall t \geq 0 \\ 0, & s > s_0, \quad \forall t \geq 0. \end{cases} \tag{2.27}$$

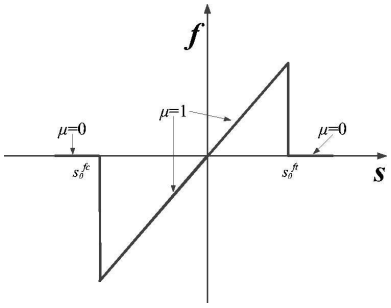

Figure 2.4: Fracture occurs when the bonds are broken and the breaking point is determined by the macroscopic mechanical properties of the material. In this sketch, the value of the scalar function λ is represented by μ. It becomes equal to 0 when the failure takes place.

The value of the scalar function is taken into account in equation (2.24). The pairwise density function $\boldsymbol{f}(\boldsymbol{X}_0', \boldsymbol{X}_0, t)$ is directly nullified when the bond is broken. If the value of the bond stretch returns to be lower than the limit, once the interaction between two points is disabled, the two particles involved can no longer interact with each other. Let's examine two material particles $\boldsymbol{X}_0$ and $\boldsymbol{X}_0'$, located between a fracture in a brittle micro-elastic material as shown in figure 2.5. The work needed to break to bond ξ that connects the two material points is:

$$w_0(\xi) = \int_0^{s_0} c_0 s r \; ds = \frac{1}{2} c_0 s_0^2 r \tag{2.28}$$

where $r = ||\xi||$. About the figure 2.5 and considering a spherical coordinate system; the work W_0 necessary to break all the bonds linking the material points $\boldsymbol{X}_0$ and $\boldsymbol{X}_0'$, can be computed as:

$$W_0 = \int_0^s \int_0^{2\pi} \int_z^{\delta} \int_0^{cos^{-1}(z/r)} \left(\frac{1}{2} c_0 s_0^2 r \right) r^2 \, sin(\Phi) \, d\Phi \, dr \, d\theta \, dz \tag{2.29}$$

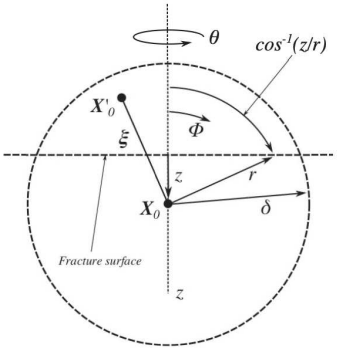

Figure 2.5: Two material points located on two sides opposite the fracture. The work to break the bonding force between the two particles is calculated by the integral equation (2.29) using a spherical coordinate system in $\boldsymbol{X}_0$.

The computation of the integral gives the following result:

$$W_0 = \frac{\pi c_0 s_0^2 \delta^5}{10} = G_0 \tag{2.30}$$

that is the energy for the part unit fracture area for complete separation of the halves of the body. The value of s_0 [16], the limit bond stretch, can be calculated by solving equation (2.29) and utilizing the values of c_0 in (2.26):

$$s_0 = \begin{cases} \sqrt{\frac{4\pi G_0}{9E\delta}}, & \text{in 2D plane-stress conditions,} \\ \sqrt{\frac{5\pi G_0}{12E\delta}}, & \text{in 2D plane-strain conditions,} \\ \sqrt{\frac{5G_0}{6E\delta}}, & \text{in 3D.} \end{cases} \tag{2.31}$$

In this framework, the introduction of damage at the bond level leads to a clear notion of local damage at a point, identified as *damage level*:

$$\Phi(\boldsymbol{X}_0, t) = 1 - \frac{\int_{\mathcal{H}_{X_0}} \lambda(\xi, t) dV'}{\int_{\mathcal{H}_{X_0}} dV'.} \tag{2.32}$$

The damage level is a function of the position of the body, and it is a scalar-valued function $0 \leq \Phi \leq 1$, in which 0 represents the material without any damage, the connections between the point and the surrounding environment are intact and 1 corresponds to a fracture in the material and therefore to a disconnection of the bonds. In the peridynamics model, a bond rupture between two points means local damage: that is, a micro-crack that propagates in a normal direction of the broken bond. In these terms, the bond fracture

locally affects the balance of internal force, the stress and the weakening of the material are automatically reproduced, by the model, at the crack tips. The bonds can no longer sustain tension load and lead to a softening of the material response, which causes the evolution and extension of the breaking through the surface.

2.4 Discretization of peridynamic equation

The theory of peridynamic is based on the concept of subdivision of the solid body into a set of finite-size material particles, or discrete particles; these terms denote the discrete counterpart of the material point: a small area of the material nearby a material point and centered in it. On the contrary, of the material point that has neither mass nor volume (they are zero), a discrete particle has a fixed finite mass and volume. Different discretization strategies can be employed; in this thesis, the solid object is discretized via finite Cartesian distribution of finite-size cubes N_p and discrete equispaced material particles, with Δ_s the node spacing (which is equal to the node edge size and is the same in the x,y, and z directions) as sketched in figure 2.6. A computational node is located on the geometric centroid of each finite-size particle, and the ratio between the horizon and the particle size is defined as $m = \delta/\Delta_s$.

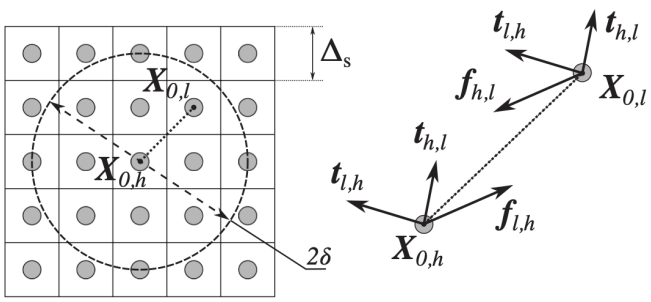

Figure 2.6: A discretized peridynamic solid, in the 2D case; the diagram on the right shows the two material points with their force density vectors.

Relating to the figure above (2.6), the variable $\boldsymbol{X}_{0,h}$ refers to the particle centroid coordinates in the Lagrangian configuration of the body, with $1 \leq h \leq N_p$; in the continuum case, the same variable will be used to denote the material particle itself. The two Lagrangian variables $\boldsymbol{X}_h(\boldsymbol{X}_{0,h}, t)$ and $\boldsymbol{V}_h(\boldsymbol{X}_{0,h}, t)$, in a deformed configuration, refer respectively to the position and velocity of the centroid of the material particle quantified at time $t \geq 0$.

The vector $\xi_{h,l}$ denotes the bond connecting material point $\boldsymbol{X}_{0,h}$ to $\boldsymbol{X}_{0,l}$ in the reference configuration of the body, whereas, $\zeta_{h,l}$ denotes the same bond in its deformed configuration at a generic time t; $\eta_{h,l}$ is the bond displacement vector:

$$\xi_{h,l} = \boldsymbol{X}_{0,l} - \boldsymbol{X}_{0,h} \tag{2.33}$$

$$\zeta_{h,l} = \boldsymbol{X}_{l} - \boldsymbol{X}_{h} \tag{2.34}$$

$$\eta_{h,l} = (\boldsymbol{X}_{l} - \boldsymbol{X}_{h}) - (\boldsymbol{X}_{0,l} - \boldsymbol{X}_{0,h}) \tag{2.35}$$

In the discrete case, it is appropriate to rewrite the definition of neighborhood, introduced in the continuum case by equation (2.1); in this term, the discrete representation of the surroundings and spatial accuracy of integration are improved:

$$\mathcal{H}_{\boldsymbol{X}_{0,h}} = \left\{ \boldsymbol{X}_{0,l} \in \mathcal{B}, ||\boldsymbol{X}_{0,l} - \boldsymbol{X}_{0,h}|| < \delta + \frac{1}{2}\Delta_s \right\} \tag{2.36}$$

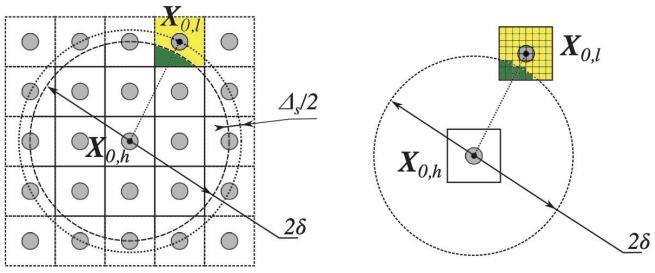

Figure 2.7: Left panel: two-dimensional schematic of the discretization of a solid in peridynamic showing the neighborhood defined by the equation (2.36.) Right panel: pairwise interaction between a couple of finite-size material particles. The green region shows the portion of the volume $\boldsymbol{X}_{0,l}$ enclosed into the sphere of radius δ centered at $\boldsymbol{X}_{0,h}$.

The region, in the discrete peridynamics formulation, is discretized into nodes, each with a known volume in the reference configuration, and the computation of integrals over a particle's neighborhood $\boldsymbol{X}_{0,h}$, is given as a summation over its discrete contributions. Under these hypotheses, the motion of each node, belonging to an arbitrarily shaped solid object, is described by the following Lagrangian equation for any $\boldsymbol{X}_{0,h}$ particle:

$$\rho_s(\boldsymbol{X}_{0,h})\frac{d^2\boldsymbol{X}_h}{dt^2} = \sum_{l=1}^{N_h}(\boldsymbol{t}_{h,l} - \boldsymbol{t}_{l,h})\Gamma_{h,l}\Delta V_l + \boldsymbol{F}_h + \boldsymbol{C}_h + \boldsymbol{D}_h, \tag{2.37}$$

$$\frac{d\boldsymbol{X}_h}{dt} = \boldsymbol{V}_h, \tag{2.38}$$

where ρ_s is the density of the solid, $\boldsymbol{X}_h$ and $\boldsymbol{V}_h$ are the Lagrangian position and velocity of the considered node. The summation is taken over the neighborhood of $\boldsymbol{X}_{0,h}$, $\mathcal{H}_{\boldsymbol{X}_{0,h}}$, which contains N_h material nodes belonging to the horizon sphere, whereas $\boldsymbol{t}_{h,l}$ and $\boldsymbol{t}_{l,h}$ represent the bond force density vectors related to the two material nodes ($\boldsymbol{t}$ and $\boldsymbol{t}'$ in the continuum case). In addition, there are two distinct forms of external forces per unit volume acting on $\boldsymbol{X}_{0,h}$: the term $\boldsymbol{F}_h$ refers to the force density per unit volume acted on the center node by the fluid flow and $\boldsymbol{C}_h$ indicates the force per unit volume arising from a solid-solid contacts or solid boundaries. The term $\boldsymbol{D}_h$ instead, represents an internal damping force that introduces a dynamic dissipation to the motion model of the peridynamic solid. This is a self-balancing internal force, depending on the relative velocity between the pairs of discrete particles. In this sense, it is a force that does not affect the motion of the rigid body of the solid or the low frequency modes; such that in high frequency simulations, they are filtered and ignored. It is worth dwelling on the parameter $\Gamma_{h,l}$ defined as the volume reduction factor. This term takes into account the volume reduction of a particle that has interactions with the boundary neighborhood, or takes into account that only a fraction of the volume containing the $\boldsymbol{X}_{0,l}$ particle, that could be enclosed into the sphere of radius δ centered in $\boldsymbol{X}_{0,h}$, as represented in figure 2.7. The parameter $\Gamma_{h,l}$ indicates the ratio of the volume fraction of $\boldsymbol{X}_{0,l}$ within a distance δ from $\boldsymbol{X}_{0,h}$ the total volume of $\boldsymbol{X}_{0,l}$. The value of $\Gamma_{h,l}$, in two-dimensional cases, is determined by a linear variation between 1/2 and 1, based on the particle's position with respect to the horizon [19] [27], δ:

$$\Gamma_{h,l} = \begin{cases} \frac{\delta - ||\xi_{h,l}||}{\Delta_s} + \frac{1}{2}, & \left(\delta - \frac{\Delta_s}{2}\right) \leq ||\xi_{h,l}|| \leq \delta, \\ 1, & 0 \leq ||\xi_{h,l}|| \leq \left(\delta - \frac{\Delta_s}{2}\right). \end{cases} \tag{2.39}$$

In equation (2.37), ΔV_l refers to the entire volume of the $\boldsymbol{X}_{0,h}$ material particle, in this specific case the discretization of the material is through cubes, so $\Delta V_l = \Delta_s^3$. It should be noted that the $\Gamma_{h,l}$ value does not depend on time and is estimated in the body reference configuration. The equation (2.39) is only applicable to the two-dimensional scenario, in the three-dimensional case, there are no analytical formulas, and $\Gamma_{h,l}$ must be computed numerically. Lastly, on the issue of convergence in the peridynamic of a continuum mechanics problem, it has been established that the solutions of a discrete peridynamic model converge to the classical elastic solutions for $\delta \to 0$ (delta-convergence)

and $m \to \infty$ (m-convergence), which are two fundamental conditions.

2.4.1 Discrete bond-based peridynamics

For the discrete case in the bond-based peridynamic model the equations (2.37)-(2.38) can be reformulated, applying the relationship between the two material particles as the pairwise density function and bond force densities:

$$\rho_s \frac{d^2 \boldsymbol{X}_h}{dt^2} = \sum_{l=1}^{N_h} \boldsymbol{f}_{h,l} \Gamma_{h,l} \Delta V_l + \boldsymbol{F}_h + \boldsymbol{C}_h + \boldsymbol{D}_h, \tag{2.40}$$

$$\frac{d\boldsymbol{X}_h}{dt} = \boldsymbol{V}_h, \tag{2.41}$$

where $\boldsymbol{f}_{h,l}$ is the discrete pairwise density function. It is dependent on the macroscopic properties of the material, its bond stretch $s_{h,l}$, and the scalar-value function $\lambda_{h,l}$:

$$\boldsymbol{f}_{h,l} = c_0 \lambda_{h,l} s_{h,l} \frac{\xi_{h,l} + \eta_{h,l}}{||\xi_{h,l} + \eta_{h,l}||}. \tag{2.42}$$

All the equations, for the parameters, are provided in the above sections, and they must be referred to the bond between the two particles $\boldsymbol{X}_{0,h}$ and $\boldsymbol{X}_{0,l}$, in conclusion, the bond micro-modulus c_0 is assumed to be constant.

2.4.2 Interface Detection and Solid–Solid Contact Forces

A discretized continuum, in the Lagrangian structure, as seen in the previous paragraphs, is represented as a set of finite-size material particles. The problem consists of identifying and tracing the interface that separates the solid space from the surrounding space. A solution consists of the implementation of Lagrangian markers distributed along the solid surface, solidly, which trace the solid-space the surrounding interface. In particular, Lagrangian interface markers consist of a subset of material particles selected, determined on a prescribed criterion from the whole set of particles constituting the solid, which are located on the surface of the solid. In this sense:

- the interfaces are mapped automatically using the Lagrangian equations of peridynamics;
- new interfaces are generated and new material particles are employed as markers as a consequence of crack formation.

The basic concept is to assume that the particle is positioned in the interface if there is a region of surrounding area that is devoid of other particles that interact with that considered, that is, the particle has no bonds. In the opposite case, the particle is considered to be the internal part of the body. In particular,

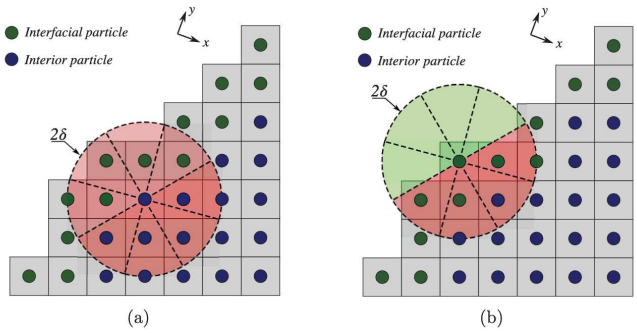

Figure 2.8: Left panel (a): Material node $\boldsymbol{X}_h$ is located in the solid interior. Right panel (b): Material node $\boldsymbol{X}_h$ is located on the interface.

the interface detection criterion proposes two conditions, which can be satisfied individually or simultaneously, for which the central particle $\boldsymbol{X}_{0,h}$ is considered sited on the interface. The first requirement is that at least N_v consecutive sectors are depleted of particles; the second need is that all bonds, $\xi_{h,l}$ in at least N_v arbitrary consecutive sectors are broken ($\lambda_{h,l} = 0$) and the distances $\bar{r}_{h,k}$ in each of these areas are higher than a prescribed threshold value, $\bar{r}_{thr}$. The $\bar{r}_{h,k}$ value, is defined as below:

$$\bar{r}_{h,k} = \frac{\sum_{l=1}^{N_k} ||(\boldsymbol{X}_l - \boldsymbol{X}_h)||(1 - \lambda_{h,l})}{\sum_{l=1}^{N_k}(1 - \lambda_{h,l})}, \tag{2.43}$$

where the two Lagrangian coordinates of the particles are estimated at time $t \geq 0$. As shown in figure 2.8 (b), one of the problems that can arise is the determination of the material points that reside near a boundary but are characterized by an environment in which the presence of other material points is only partial, that is, material nodes lack a complete neighborhood volume. This leads to different effective mechanical behavior of the peridynamic model of the material, in the interface zone, from that evaluated inside the solid. This event is called the *surface effect* and therefore it involves a smoothing of the material response at the free interface areas of the solid, due to the lack of bonds. Diverse approaches to solving the problem are available, the one used in this manuscript is known as the *volume method*, due to its simplicity and efficiency. The basic idea is to correct the value of the micro-modulus,

c_0, of the bonds around the node that is near the edge, increasing it with a, $\gamma_{h,l}$, dimensionless parameter called stiffening factor. In this manner, this corrects the softening of the material near the border, achieving the same strain energy density as that of an internal point, under homogeneous deformation. For further details, please refer to the bibliography article [16]. Once the interfaces have been identified, it is possible to estimate the normal, tangent, and bi-normal vectors. The unit normal vector can be computed at $\boldsymbol{X}_h$ via the following expression:

$$\boldsymbol{\eta}_h = \frac{\sum_{l=1}^{N_h}(\boldsymbol{X}_l - \boldsymbol{X}_h)\lambda_{h,l}\Gamma_{h,l}\Delta V_l}{\sum_{l=1}^{N_h}\lambda_{h,l}\Gamma_{h,l}\Delta V_l} \tag{2.44}$$

$$\hat{\boldsymbol{\eta}}_h = \frac{\boldsymbol{\eta}_h}{||\boldsymbol{\eta}_h||}, \tag{2.45}$$

where $\hat{\boldsymbol{\eta}}_h$ points to the solid interior of the surrounding fluid. Once the unit normal is known, the tangent vector, $\hat{\boldsymbol{t}}_h$ can be easily computed as well as the bi-normal vector, $\hat{\boldsymbol{b}}_h = \hat{\boldsymbol{\eta}}_h \times \hat{\boldsymbol{t}}_h$. Additional information about the procedure for computing tangent, normal, and bi-normal vectors is provided in the bibliography article [7].

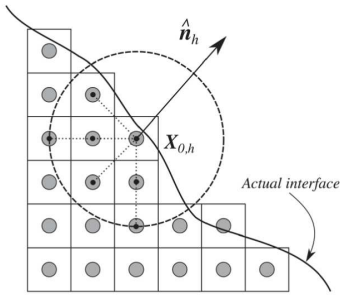

Figure 2.9: Schematic method for calculating the unit normal vector to the interface of a generic solid, $\hat{\boldsymbol{\eta}}_h$, at Lagrangian position $\boldsymbol{X}_h$.

The solid-solid contact forces are characterized by pairwise short-range forces that act between couples of peridynamic particles located within a cut-off distance, r_c. In particular, given a pair of particles, $\boldsymbol{X}_l$ and $\boldsymbol{X}_h$ the effect of short-range force due to contact of the particle $\boldsymbol{X}_l$, on the particle, $\boldsymbol{X}_h$ is :

$$\boldsymbol{C}_{h,l} = max\left\{k_c\left[\left(\frac{r_c}{||\boldsymbol{\zeta}_{h,l}||}\right)^{n_c} - 1\right], 0\right\}\frac{(\boldsymbol{X}_l - \boldsymbol{X}_h)}{||(\boldsymbol{X}_l - \boldsymbol{X}_h)||}, \tag{2.46}$$

where $\boldsymbol{\zeta}_{h,l}$ is the distance between the particles (equation 2.34), n_c is a shot-range force exponent and k_c is a short-range force constant. In the peridynamic

contact model the parameters n_c, r_c, and k_c represent fundamental parameters and as demonstrated by Macek and Silling (2007) [17], among other possibilities, the values of these constants can be set to $n_c = 1$, $k_c = 15c_0$ and $r_c = \Delta_s$, with c_0 the bond micro-modulus defined by equation (2.26) and Δ_s the mean spacing between material particles [7].

2.5 Numerical Method

This section discusses the coupling procedures between the governing equations of peridynamics and the equations for the Navier-Stokes incompressible fluid through the use of the Immersed Boundary Method (IBM) approach, idealized by Breugom [3] and the normal probe method of Wang et al. [36]. The equations are solved within a massively parallel numerical solver based on the Message Passing Interface (MPI). The solution is derived through a main module that solves the dynamic fluid equations, based on the open-source solver CANS by Costa [5], coupled to a segregated solver for the governing peridynamics equations. The dynamics of the code are such that variations caused by fluid-structure interaction, such as crack formation or solid breakage, can be taken into account in a 3D view.

2.5.1 Governing equations of fluid dynamics

In the framework of FSI problems, the incompressible formulation of the Navier-Stokes equations is used for the numerical description of the mechanical behavior of the fluid phase [24]:

$$\nabla \cdot \boldsymbol{u} = 0 \tag{2.47}$$

$$\rho_f \left(\frac{\partial \boldsymbol{u}}{\partial t} + \boldsymbol{u} \cdot \nabla \boldsymbol{u} \right) = -\nabla p + \mu_f \nabla^2 \boldsymbol{u} + \rho_f \boldsymbol{q}, \tag{2.48}$$

where $\boldsymbol{u}$ is the fluid velocity field, p the hydrodynamic pressure, μ_f the dynamic viscosity and ρ_f the density of the fluid phase, where $\boldsymbol{q}$, in the right-hand, represents the forcing term, from the IB method. The equations are calculated on a rectangular computational domain. The Eulerian domain is discretized by a Cartesian grid with cubic cells equi-spaced, in its configured reference, with Δ_f spacing. For an initial configuration, the size of the Eulerian grid cells and the distance between the Lagrangian particles are set equal, $\Delta_s = \Delta_f$. This means, that as time and fluid motion advance, the Eulerian grid remains fixed during the simulation, while the nodes of the solid can only move within the

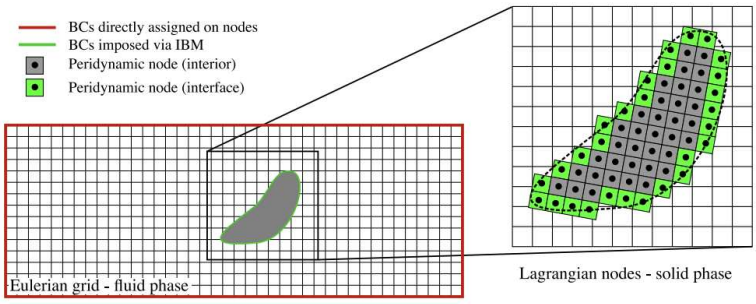

Figure 2.10: 2D schematic sketch of Eulerian domain and Lagrangian solid discretization. The red line represents the area where boundary conditions are assigned directly on the nodes using ghost nodes. While, the green line shows the area of the solid-structure interface where the immersed boundary method is applied.

domain, changing position and relative distance between them if the fracture of the solid occurs. The boundary conditions are imposed in the Eulerian grid side by ghost nodes, while in the case of the solid-fluid interfaces, the discrete-forcing method is applied, such as the immersed boundary method, which imposes the conditions of no-penetration and no-slip on the borders.

2.5.2 Computation of the hydrodynamic forces and viscous stresses

In the frame of IB methods, different approaches have been proposed in order to determine the forces that arise from the interaction of the fluid with the solid surface. Among these are highlighted the *normal-probe method* [10] [36] [32] and the integration of the IBM forcing, $\boldsymbol{q}$, on the solid body interfaces [3]. Although the latter is the most widely used, this approach does not allow for the calculation of the stress distribution, which knowledge is necessary to know the state of deformation of the deformable solid. Furthermore, the equation on which this method is based, is not achievable on discrete surface elements, as it would lead to problems regarding the removal of forces due to the internal fluid, that is, the fluid that is localized within the immersed contours but is not actually present as that space is occupied by the solid. For these reasons, the direct model of the normal-probe is adopted, in which the response of the solid to the presence of the fluid is evaluated via the computation of hydrodynamic pressure and viscous stresses near the fluid-solid interface. In this regard, normal vectors, evaluated in equations (2.44)-(2.45), tangents, and bi-normal in the interface must be known a priori. It is necessary to consider an orthogonal local coordinate system with axes $(\xi - \eta - \zeta)$ arranged along

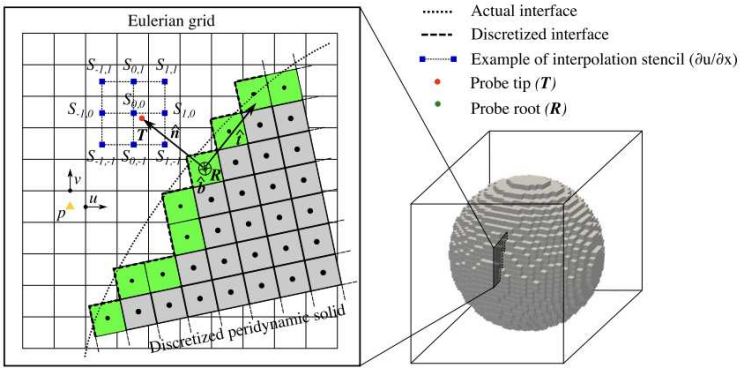

Figure 2.11:

the tangent, normal, and bi-normal vector directions, respectively. At each Lagrangian, $\boldsymbol{X}_h$, material node, located in the solid-fluid boundary, a probe is sent along the direction of the normal vector. The length of the probe is measured as $l = 2\Delta_f$ [36]. By naming $\mathbf{T}$ and $\mathbf{R}$, respectively, the tip and the root of the probe then the pressure is extrapolated to the point at the root, according to Wang et al. [36]:

$$p|_R = p|_T + \frac{1}{2}\left[\left.\frac{\partial p}{\partial \eta}\right|_R + \left.\frac{\partial p}{\partial \eta}\right|_T\right] l, \tag{2.49}$$

$$\left.\frac{\partial p}{\partial \eta}\right|_R \approx \left.\frac{D\boldsymbol{u}}{Dt}\right|_R \left.\frac{\partial p}{\partial \eta}\right|_R \approx \frac{d\boldsymbol{U}_h}{dt} \cdot \hat{\boldsymbol{n}}_h, \tag{2.50}$$

$$\left.\frac{\partial p}{\partial \eta}\right|_T = \nabla p|_T \cdot \hat{\boldsymbol{n}}_h, \tag{2.51}$$

$$p|_T = \sum_{I,J,K} = p|_{\boldsymbol{S}_{I,J,K}} \delta_\Delta(\boldsymbol{S}_{I,J,K} - \boldsymbol{X}_T)\Delta_f^3. \tag{2.52}$$

where the pressure gradient $\nabla_p|_T$ is computed via the central finite difference scheme on the stencil as represented in figure 2.11 for the two-dimensional case. The indexes I, J, and K refer to the coordinates of a generic node of the proper interpolation stencil $\boldsymbol{S}_{I,J,K}$. The fluid pressure is computed on each node of the stencil by equation (2.52), and all interpolation operations are developed on the regularized Direct delta function, δ_Δ, defined according Roma et al. [23], on the next page.

$$
\begin{aligned}
&\delta_\Delta(\boldsymbol{x}-\boldsymbol{x}_0) = \delta'_\Delta(x-x_0)\delta'_\Delta(y-y_0)\delta'_\Delta(z-z_0)\\
&\delta'_\Delta(s-s_0) = \frac{1}{\Delta_f}\Phi\left(\frac{s-s_0}{\Delta_f}\right)\\
&\Phi(a) = \begin{cases} \frac{1}{3}\left(1+\sqrt{1-3a^2}\right), & a \le 0.5,\\ \frac{1}{6}\left(5-3|a|-\sqrt{1-3(1-|a|)^2}\right), & 0.5 < |a| \le 1.5\\ 0, & |a| > 1.5. \end{cases}
\end{aligned}
\tag{2.53}
$$

Following these considerations, it is possible to calculate the shear stress measured at the probe root, **R**, which depends on the velocity gradient calculated at the probe tip, **T**. The velocity derivatives expressed in the local frame of reference evaluated at the probe root, **R**, read:

$$\left.\frac{\partial u_\xi}{\partial \eta}\right|_R = \nabla \boldsymbol{u}|_T \cdot \hat{\boldsymbol{t}} \cdot \hat{\boldsymbol{n}}, \tag{2.54}$$

$$\left.\frac{\partial u_\zeta}{\partial \eta}\right|_R = \nabla \boldsymbol{u}|_T \cdot \hat{\boldsymbol{b}} \cdot \hat{\boldsymbol{n}}, \tag{2.55}$$

$$\left.\frac{\partial u_\eta}{\partial \eta}\right|_R = \nabla \boldsymbol{u}|_T \cdot \hat{\boldsymbol{n}} \cdot \hat{\boldsymbol{n}}. \tag{2.56}$$

It is worth remembering that the above equations apply only in the condition of a linear velocity field in the vicinity of the solid-fluid interface. This assumption is observed when the grid is sufficiently small to solve the equations in the boundary layer near the edge. The stress elements expressed in the local reference frame are:

$$\tau_\xi = \mu \left.\frac{\partial u_\xi}{\partial \eta}\right|_R \tag{2.57}$$

$$\tau_\zeta = \mu \left.\frac{\partial u_\zeta}{\partial \eta}\right|_R \tag{2.58}$$

$$\tau_\eta = \mu \left.\frac{\partial u_\eta}{\partial \eta}\right|_R - p|_R. \tag{2.59}$$

It follows that the stress components can be expressed in the global frame of reference (x, y, z):

$$\begin{bmatrix} \tau_x \\ \tau_y \\ \tau_z \end{bmatrix} = \begin{bmatrix} \hat{t}_x & \hat{n}_x & \hat{b}_x \\ \hat{t}_y & \hat{n}_y & \hat{b}_y \\ \hat{t}_z & \hat{n}_z & \hat{b}_z \end{bmatrix} \begin{bmatrix} \tau_\xi \\ \tau_\eta \\ \tau_\zeta \end{bmatrix}. \tag{2.60}$$

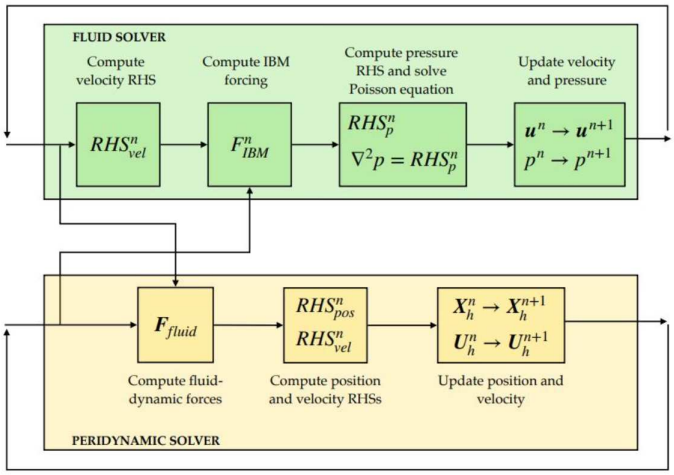

Figure 2.12: Scheme of the weak-coupling program.

In conclusion, in the global reference system, the force per unit volume that the liquid exerts on the solid, at the Lagrangian position $\boldsymbol{X}_h$, can be reported:

$$\boldsymbol{F}_h = -\boldsymbol{\tau}_h \frac{A_h}{\Delta s^3}, \tag{2.61}$$

where A_h is a fixed area, and denotes the actual surface area of the discrete particle, $\boldsymbol{X}_h$. It is evaluated at the beginning of the simulation as the concrete area of the solid divided by the number of the total number of the interfacial material particles, while $\boldsymbol{\tau}_h$ is the total stress expressed in the global frame of reference. The value of A_h is set to $A_h = \Delta_s^{2/3}$. The same value is used for the area of the new interfacial particles that occur as a result of the fracture of the solid. It is worth noting that a new fluid region is also formed when the new surface is generated due to the break. In the first phase of the formation, the gap has a size comparable to the Eulerian cells or smaller, and the computation of the hydrodynamic force via equation (2.61) is inaccurate. In this respect, to mitigate this issue, the algorithm for the determination of the interface implements a control, on the peridynamic particles subject to broken bonds. The hydrodynamic force is calculated in the Lagrangian nodes of the particles when the gap is larger than three Eulerian cells. If the value of the gap is smaller, the particles are considered the inner part of the body and the force is not calculated.

2.5.3 Coupled fluid-structure interaction algorithm

The peridynamic governing equations (2.40)-(2.41) are coupled to the Navier-Stokes equations (2.47)-(2.48), in the frame of an explicit, weak coupling scheme in figure 2.12. The multi-direct forcing Immersed Boundary Method, by Breugem (2012) [3], is implemented to apply the no-penetration and no-slip conditions to the flow phase in the solid-fluid interface. All spatial and temporal scales are directly resolved through direct numerical simulations. In addition, the staggered grid method is used to avoid pressure-velocity decoupling. That is, the scalar quantities (pressure, temperature..) are supposed to live at the center of the cell, while the vector quantities (velocity) are defined at the edge of the cell. The Navier-Stokes equations are solved using a pressure-correction approach, via second-order finite difference element schemes for space discretization and the third Runge-Kutta time marching algorithm. Those are advanced in time from t^n to t^{n+1} on the fixed Cartesian grid, with a time step Δt_f. In a different manner, the solid phase is resolved by a segregated solver based on a Verlet time marching scheme. As outlined in figure 2.12, the solid positions and velocities at the time step t^n are passed to the fluid phase solver from the segregated solver to compute the forces acted by the fluid flow on the solid. Then, this information is transmitted to the segregated solver, which evolves the peridynamic equations over the same interval of time, Δt_f, though a sub-stepping procedure with a time step $\Delta t_s < \Delta t_f$. After this procedure, the displacement values are sent to the main solver to repeat the whole process.The algorithm is provided below:

do for r = 1,3,

$$\boldsymbol{u}^* = \boldsymbol{u}^{\boldsymbol{r-1}} + \frac{\Delta t}{\rho_f}\big(\alpha_r \boldsymbol{FRHS}^{r-1} + \beta_f \boldsymbol{FRSH}^{r-2} - \gamma_r \nabla p^{r-3/2}\big), \tag{2.62}$$

$$\hat{\boldsymbol{u}} = \boldsymbol{u}^* \tag{2.63}$$

do for $s = 1, N_s$,

do for $h = 1, N_p$,

$$\hat{\boldsymbol{U}}_h^{s-1} = \sum_{i=1}^{N_x}\sum_{j=1}^{N_y}\sum_{k=1}^{N_z} \hat{\boldsymbol{u}}_{i,j,k}^{s-1}\delta_\Delta\big(\boldsymbol{x}_{i,j,k} - \boldsymbol{X}_h^n\big)\Delta_f^3, \tag{2.64}$$

$$\boldsymbol{Q}_h^{r-1/2,s} = \boldsymbol{Q}_h^{r-1/2,s-1} + \frac{\boldsymbol{V}_h^n - \hat{\boldsymbol{U}}_h^{s-1}}{\Delta_h}, \tag{2.65}$$

end do,

do for $[i,j,k]$=[1,1,1],$[N_x, N_y, N_z]$,

$$\boldsymbol{q}_{i,j,k}^{r-1/2,s} = \sum_{h=1}^{N_p} \boldsymbol{Q}_h^{q-1/2,s} \delta_\Delta\big(\boldsymbol{x}_{i,j,k} - \boldsymbol{X}_h^n\big)\Delta V_h, \tag{2.66}$$

$$\hat{\boldsymbol{u}}_{i,j,k}^{s} = \boldsymbol{u}_{i,j,k}^{*} + \Delta t\ \boldsymbol{q}_{i,j,k}^{r-1/2,s}, \tag{2.67}$$

end do,

end do,

$$\nabla^2 \hat{p} = \frac{\rho_f}{\gamma \Delta t_f} \nabla \cdot \boldsymbol{u}^*, \tag{2.68}$$

$$\boldsymbol{u}^r = \boldsymbol{u}^* - \frac{\gamma_r \Delta t}{\rho_f} \nabla \hat{p}, \tag{2.69}$$

$$p^{r-1/2} = p^{r-3/2} + \hat{p}, \tag{2.70}$$

do for $r = 1, 3$,

do for $h = 1, N_p$,

$$\boldsymbol{X}_h^r = \boldsymbol{X}_h^{r-1} + \Delta t_s \left(\alpha_r \boldsymbol{V}_h^{r-1} + \beta_r \boldsymbol{V}_h^{r-2} - \gamma_r \boldsymbol{V}_h^{r-3}\right), \tag{2.71}$$

$$\boldsymbol{V}_h^r = \boldsymbol{V}_h^{r-1} + \frac{\Delta t_s}{\rho_s}\big(\alpha_r \boldsymbol{PRHS}_h^{r-1} + \beta_r \boldsymbol{PHRS}_h^{r-2} - \gamma_r \boldsymbol{PHRS}_h^{r-3}\big), \tag{2.72}$$

end do,

end do.

The algorithm can be divided into three large blocks. The first block, equations (2.62)-(2.63) and equations (2.68)-(2.70), computes the velocity for the Navier-Stokes equations in a logic of pressure-correction. For the estimation of a first velocity, denoted as first prediction velocity, the right-hand side of equation (2.48) is modified, $\boldsymbol{FRSH} = -\rho_f \boldsymbol{u} \cdot \nabla \boldsymbol{u} + \mu_f \nabla^2 \boldsymbol{u}$, is used, together with the pressure, for the approximation of the velocity. The velocity field is a non-solenoidal approximation and it must be projected to obtain the divergence-free velocity at time step t^{n+1}, $\boldsymbol{u}^{n+1}$. The pressure-correction method predicts that the integration of the incompressible Navier-Stokes equations is done in sub-steps, so the superscript r refers to each sub-step of the iterative Runge-Kutta cycle, and corresponds to the time t_n for $r = 0$ and t_{n+1} for r=3. Moreover the coefficients α_r, β_r and γ_r are the Runge-Kutta coefficients provided in the following table 2.1, on the next page. The variable $\hat{\boldsymbol{u}}$ is second the prediction velocity and accounts for the effect of the forcing, $\boldsymbol{q}$. The force term and the second prediction of the velocity field are computed at the second block, equations (2.64)-(2.67). In this regard, the forcing term $\boldsymbol{q}$ is determined according to an interactive scheme referred to as *multi-direct forcing* [3]. The superscript s refers to each sub-step to iterative procedure,

	r=1	r=2	r=3
α_r	8/15	5/12	3/4
β_r	0	-17/60	-5/12
γ_r	8/15	2/15	1/3

Table 2.1: Runge-Kutta coefficients α_r,β_r and $\gamma_r = \alpha_r + \beta_r$ used for the time marching Rungr-Kutta scheme tabled versus the sub-step index, r

with $\hat{\boldsymbol{u}}^0 = \boldsymbol{u}^*$. At the Lagrangian position $\boldsymbol{X}_h^{r-1}$, the second prediction velocity field of the fluid, $\hat{\boldsymbol{u}}^s$, is named the Lagrangian variable $\hat{\boldsymbol{U}}_h^s$, evaluated at time level t^{r-1} in each solid material particle located in the solid-fluid interface. Then as well, the term of the Lagrangian force $\boldsymbol{Q}_h^{r-1/2,s}$ is computed at the time step $t^{r-1/2}$. According to the equation (2.65), the $\boldsymbol{Q}_h^{r-1/2,s}$ force is given by the ratio between $\boldsymbol{V}_h^n - \hat{\boldsymbol{U}}_h^{s-1}$ and the time step used for the principal loop. The parameter $\boldsymbol{V}_h^n$ is the velocity evaluated at time step t^{r-1} on $\boldsymbol{X}_{0,h}$ node. In the last step of the second block, the Lagrangian quantity $\boldsymbol{Q}_h^{r-1/2,s}$ is spread on the Eulerian grid, in order to estimate the forcing term $\boldsymbol{q}^{r-1/2,s}$, for every material node. In conclusion it is possible, using the updated prediction velocity $\boldsymbol{u}^*$, to re-computed the prediction velocity, $\hat{\boldsymbol{u}}^s$ for each node of the Eulerian grid. The number of the iterations, N_s, is given by a threshold on the error on the imposition of the velocity at the fluid-solid interface. Therefore, in general, to obtain a second order of accuracy for the measurement of the velocity on the solid-fluid border is sufficient to set the value $N_s = 2$. At this point, the boundary conditions are imposed via the immersed boundary procedure, and the Poisson's pressure equation is solved. The velocity and pressure fields are advanced using the value of pressure $\hat{p}$, and the solution of the solid phase is synchronized to the fluid one via a sud-stepping procedure. The last block, equations (2.71)-(2.72), is an explicit Runge-Kutta marching scheme used for the temporal integration of equations (2.38)-(2.39). The superscript r refers to the steps of Runge-Kutta iteration and coincides with the time level t_n for $r = 0$, and t_{n+1} for $r = 3$, with the time step size $\Delta t_s = t_{n+1} - t_n$. The equation (2.37) is used to calculate the right-hand term $\boldsymbol{PRHS}$:

$$\boldsymbol{PRHS}_h = \sum_{l=1}^{N_h} (\boldsymbol{t}_{h,l} - \boldsymbol{t}_{l,h}) \Gamma_{h,l} \Delta V_l + \boldsymbol{F}_h + \boldsymbol{C}_h + \boldsymbol{D}_h \qquad (2.73)$$

where the bond force density $\boldsymbol{t}_{h,l}$ can be designated by the constitutive bond-based model described in the 2.3.3 section. For the imposition of boundary

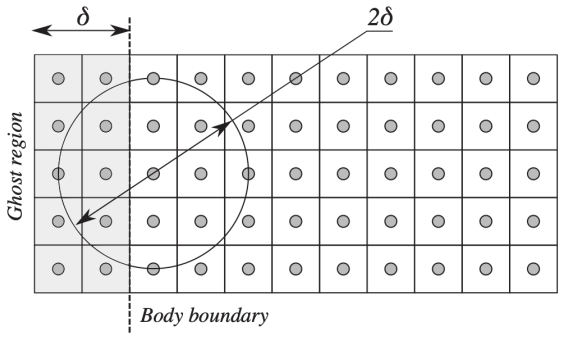

Figure 2.13: Representation of the ghost layer extension used for imposing boundary conditions. The velocity and displacement of ghost nodes are updated for each time step of the integration scheme

conditions, ghost nodes are used, distributed along the border of the solid peridynamic body, imposing a specific displacement and velocity. The extension of the ghost layer must be equal to the size of the horizon δ, so as to ensure that conditions are imposed exactly on the region of the material [16] [19], as delineated in figure 2.13. It is worth recalling that all interpolation and spreading operations are based on the regularized Direct delta function, δ_Δ, defined according to Roma et al. [23] and detailed by equation (2.53). This particular mathematical function has the width of three grid cells, which replaces the sharp interface with a thin porous shell. The porous interface has effects on the drag force of the fluid phase, as it increases the (external) radius of the spherical particles from R to $R + 3\Delta x/2$, which leans to increase the drag force. On the other hand, the porosity wall tends to decrease the drag force, at least in the area closest to the interface when the flow is laminar. The first effect is stronger than the last, with the consequence that the effective radius of the particle is larger than the actual diameter when Lagrangian makers are located exactly on the surface of the particle. In this situation, to correct this effect, the Lagrangian grid is retracted inward [3]. For more information, the reader consult the bibliography article [3].

CHAPTER 3

Simulation and Analysis

3.1 CaNS

CaNS is an open-source software developed by P. Costa [5] that allows direct numerical simulation (DNS) based on the incompressible formulation of Navier-Stokes equations. As explained in the previous chapter:

- A Runge-Kutta scheme of order three is used to discretize the time term on the *left-hand side* of the momentum balance equation;
- The *right-hand side* of the momentum balance equation, which contains the convective and the diffusive terms, is discretized using a pressure-correction algorithm and a second-order finite difference scheme.

The software uses MPI libraries. Parallel computing is based on the concept of dividing the domain into sub-domains, each of which is analyzed separately by a single processor. It is fundamental to maintain a connection and communication between the various processors, in order to transmit the necessary information for the various calculations. In this sense, it is possible to initialize more processes simultaneously and reduce the computational cost. The effectiveness of an MPI code is evaluated in terms of time gain, quantitatively by the term *scaling factor*, defined as:

$$SF = \left(\frac{t_{ref}}{t_N} \right)_{size} \tag{3.1}$$

SF represents the ratio of the time spent completing a job with a certain number of processors taken as reference t_{ref} and the time spent completing that same job using N times the reference processors, keeping the size of the problem fixed. In principle, since $t_N = N \cdot t_{ref}$, the scaling factor should

be a straight line as the number of processors increases. In reality, however, increasing the number of processors, reduces the computing time required for the single processor, thus reducing the time of analysis, but increases the number of information that processors must communicate with each other. Communication latency overrides the effectiveness of calculation, making this kind of approach less effective.

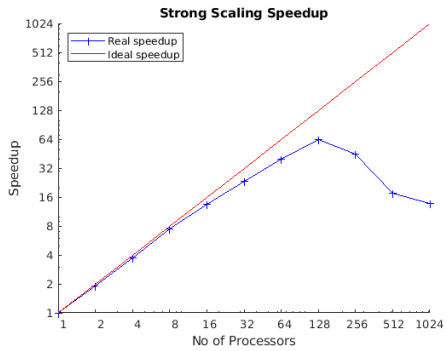

Figure 3.1: Schematic representation of scaling factor for compiling a code in which multiple processors are involved. As the number of processors increases, the theoretical trend deviates from the ideal one.

3.2 CaNS-modified

The simulations for the following manuscript employed the software CaNS-modified developed by F. Dalla Barba. The structure of the code remains the same as the original CaNS, but the difference lies in the possibility of using different numerical methods to solve the equations and the implementation of the equations of peridynamics, both in the bond-based and state-based cases, to solve the interaction of the solid phase with the fluid flow. In relation to time integration, as described in the previous chapter, an explicit Runge-Kutta method of order three is used. Explicit methods are more suitable for parallel computing, being less computationally expensive and effective, although implicit methods are known to be more stable than the latter. The use of an explicit scheme, in addition to improving the stability and accuracy of the results in this case, also represents a limit to the density ratio between solid and fluid (ρ_s/ρ_f) which ensures convergence, which is complicated when the ratio between the two densities tends to the unit value. A condition of this type is not common within problems of this type, where generally the solid has a magnitude density several orders higher than that of the fluid. For spatial in-

tegration, however, the procedure present in the basic version of the program is maintained, that is, a pressure-correction algorithm with finite difference framework of order two. The calculation domain has size $L_x \times L_y \times L_z$ respectively along the x,y and, z directions, and it is discretized using a structured and staggered Eulerian grid (fixed) equispaced along all directions, with grid size $\Delta f = \Delta x = \Delta y = \Delta z$, which coincides with the distance between the material particles ($\Delta_s = \Delta_f$) of the peridynamic theory. The procedure, as discussed in paragraph 2.5.3, is based on a sub-step division of the solid solver that computes position and velocity from the instant t_n to t_{n+1}, using a time step $\Delta t_s = R\Delta t_f$ where $R \leq 1$, $R \in \boldsymbol{R}$. The time-step used is crucial in ensuring the method's stability and effectiveness. In order to maintain smooth phase resolution stability, the limit valuable time step must be in the order of $\Delta t_f \propto \Delta_f / U_f$, where U_f is the fluid bulk velocity, while the stability of the solid solver is $\Delta t_s \propto \Delta_s / U_s$, and $U_s = \sqrt{E/\rho_s}$. Generally, $U_s \gg U_f$, the stability of the solid solver is defined in a smaller range than that of the fluid. To satisfy the stability of the whole method, the R factor is used, defined as $R = \Delta_f / \Delta_s \gg U_f / U_s$. The characteristic time scale of the solid is lower than that of the fluid, so the number of iterations required by the peridynamic time solver is higher and increase with R.

3.3 The initial simulation data

The calculation domain comprises both the fluid phase and the fibers of the material (solid phase) that are immersed in it. The two domains have distinct characteristics that are outlined below:

- Fluid domain
  - Domain size $L_x \times L_y \times L_z = 1.0 \times 0.5 \times 1.0$;
  - Laminar flow conditions at full speed;
  - A staggered structured grid of Eulerian type with $256 \times 128 \times 256$ nodes;
  - Boundary condition
    - Periodic condition for $x = x_0$ and $x = L_x$;
    - Periodic condition for $y = y_0$ and $y = L_y$;
    - Wall condition for $z = z_0$;
    - Slip-free condition for $z = L_z$;

– no-slip and no-penetration conditions at the border of the two phases, imposed as Dirichlet and Neumann conditions.

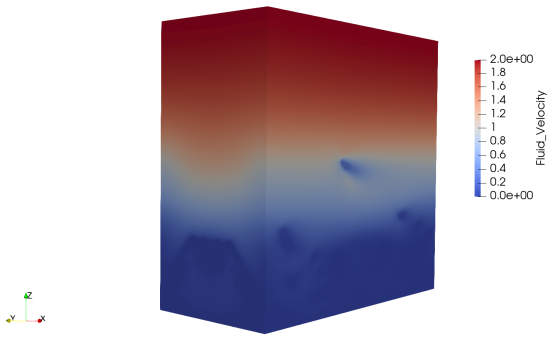

Figure 3.2: Schematic representation of the solid domain. According to the figure, there is a laminar fluid, which implies there is no vortex.

- Solid domain
  - Consisting of a block of fibers of size $L_x \times L_y \times L_z = 9.89166667^{-1} \times 4.89166667^{-1}1 \times 2.50000000^{-1}$;
  - Number of peridynamic particles 122868;
  - Dimensions of the grid type Eulerian $240 \times 240 \times 60$.

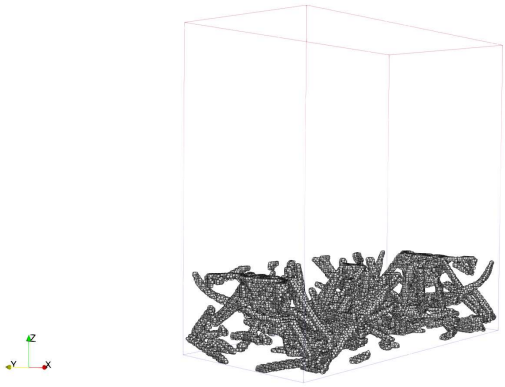

Figure 3.3: Representation of the solid domain within the fluid medium

The solid phase was obtained by X-ray tomography. The University of Illinois Urbana-Champaign provided detailed geometry of the fibers that constitute the ablative porous material. The peridynamic material is achieved by intertwining sections with a top view and executing a code in Matlab. The solid sections are represented by the images below.

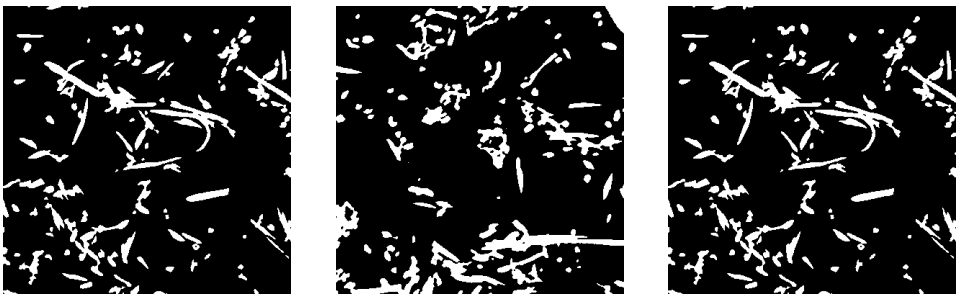

Figure 3.4: Representation of three sections of the solid obtained by X-ray tomography and used by the Matlab code to obtain the peridynamic solid.

Each pixel of the image is represented by a full space (white) that constitutes a piece of fiber, and a black space that constitutes the void. The Matlab script replaces white spaces with a peridynamic particle of radius $4.16 \cdot 10^{-3}$ (non-dimensional). The solid phase obtained using the Matlab code is depicted in figure 3.5. However, due to the significant computational cost of the entire simulation material, it was chosen to study and simulate the performance of a minor part.

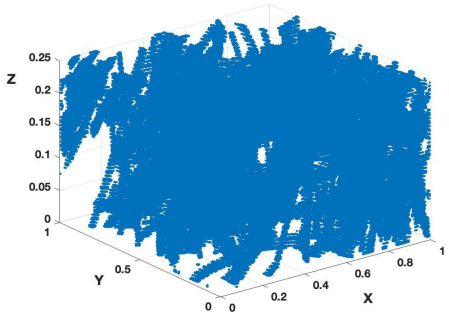

Figure 3.5: Representation of the entire solid domain obtained by the Matlab code

Due to the difficulty of the problem, it is crucial to establish parameters that lead to test convergence, such as numerical stability, density ratio, and material properties. For this type of simulation, it is essential to remember

that temporal discretization is accomplished using explicit Runge-Kutta methods while spatial discretization is done using the pressure-correction method. The numerical convergence of certain PDEs is computed using the reference parameter *Courant-Friedrichs-Lewy* (CFL). In order to maintain stability, the CFL value must be lower than the CFL_{max}, which ensures the minimum Δt required for the method to remain stable. In fact, the CFL_{max} is related to the heaviest eigenvalue which is always the most critical to stability. This parameter has a non-dimensional value and is peculiar to any method of integration.

$$CFL = \frac{u \cdot \Delta t}{\Delta x} < CFL_{max} \tag{3.2}$$

The time step Δt must be small enough to be able to describe the phenomenon and the computational cost of the operations increases if the latter is excessively reduced. The second parameter that should be examined for solving the problem is the density ratio, as indicated in the previous section. The code becomes unstable when the density ratio between solid and fluid approaches its unit value. For this reason and in order to best represent the porous solid, an elevated density ratio has been chosen. The final step in treating the problem is to examine the properties of the material, especially its *critical release of fracture energy rate*. According to the above description, the values of the parameters chosen for the simulation are:

- CFL fluid resolver: The value is set to 1 for the initialization stage, in order to maintain the fibers rigid and fixed within the domain. After initializing the simulation, its value is reduced to 0.9;
- CFL solid resolver (fibers): The value is 0.1 throughout the entire simulation process;
- Reference velocity scale: $\tilde{U} = 1.5m/s$;
- Reference length scale: $\tilde{L} = 0.1m$;
- Reference density scale: $\tilde{\rho} = 1kg/m^3$;
- Reference number for Reynold: 500.0, defined by the referred quantities specified above.

Below are listed the specific parameters for the material:

- Young's modulus : $E/(\tilde{\rho} \cdot \tilde{U}^2) = 10^5$;
- Poisson's modulus : $\nu_s = 0.25$;
- Density : $\rho/\tilde{\rho} = 800$;
- Critical fracture energy release rate : $G/(\tilde{\rho}\tilde{L}\tilde{U}^2) = 9 \cdot 10^{-4}$.

Many parameters, including material properties such as those mentioned above, were not dimensioned during the simulation. The non-dimensional approach can be useful in determining which parameters are independent and relevant, and which are negligible. In particular, the value of the critical fracture energy release rate has been determined based on preliminary analysis to ensure bonds break at a rate below 0.003%. The number of iterations performed is 70000. To accelerate the flow, the fibers of the solid are considered fixed and rigid in the first 23000 iterations. Later on, the solid can move and deform within the domain, allowing for activation of the break in the following 33200 iterations.

3.4 Analysis of the results

The simulation results allow for qualitative evaluation of the behavior of ablative material, particularly since this is a preliminary and developing study. The analysis after post-processing will focus on evaluating the qualitative extent of damage and breakage caused to solid fibers by iteration with the fluid phase. The analysis concerns on fiber displacement, stress, and fiber bond stretching level. The activation of the break of the solid occurs once the fluid has reached its regime state, as previously mentioned. Focusing on the displacement level, the following figures (figure 3.6) show different stages of the simulation performed. In order to better understand the state of the solid phase, the displacement is scaled to 0.50. The beginning and end of the simulation are represented by the first and last figure, respectively. It is important to note that the boundary conditions for the x axis are periodic, which means that everything coming out of the $x = L_x$ side falls into $x = x_0$. Upon analysis of the figures, it can be observed that the fibers that encounter the fluid first have the greatest displacement. In addition, only fibers that are not closely related to the surface located on the xy plane are moved. In fact, a wall boundary condition has been set on this surface, that is, a "non-slip" condition which assumes the speed at the wall is 0 no matter what roughness

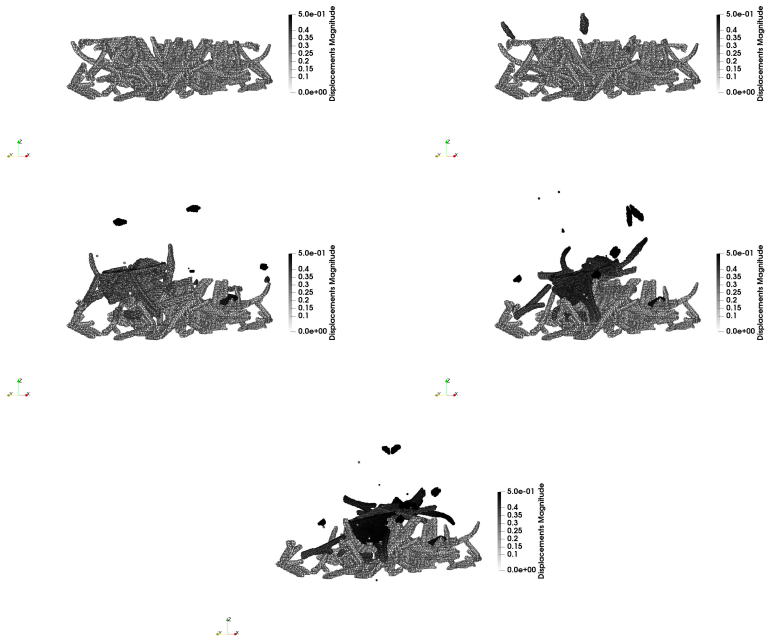

Figure 3.6: Representation of the solid displacemnent in five different stages of the simulation.

value of the wall is applied, as shown in the figure 3.7. As the temporal step progresses, the move increases until it reaches a maximum displacement of $5 \cdot 10^{-1}$ (non-dimentional). The smaller pieces of solids, that are detached first, are transported by the fluid until they reach a height of half the fluid domain. However, the larger piece remains in the lower area but it is still transported.

The investigation of displacement was followed by an analysis of the stretching of bonds between the material particles of the peridynamic solid in relation to the rate of fracture energy released per unit of area. By conducting stress and stretch analyses afterward, the orders of magnitude can be compared between fibers that experience fracture and fibers that do not experience it. It is worth remembering that in fracture mechanics, the rate of energy release (G) is the rate at which energy is transformed when a material undergoes a fracture. In mathematical terms, the rate of energy release is expressed as the decrease in total potential energy by enhancing the fracture surface, and thus is expressed in terms of energy per unit area. In this case, critical fracture energy release rate per unit area is $G_0 = 9 \cdot 10^{-4}$. The value was obtained

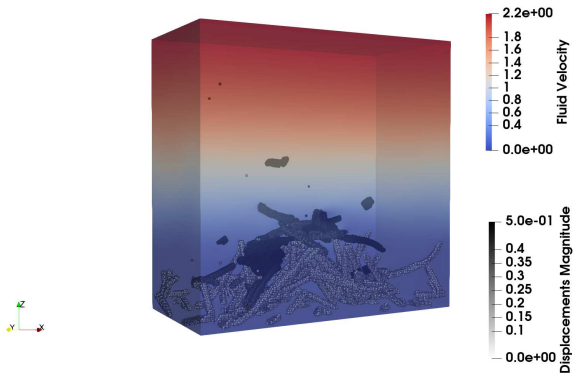

Figure 3.7: Image taken from paraview representing solid displacement and solid phase velocity.

using equation (2.31), in the three-dimensional case, employing a stretch bond limit, $s_0 = 0.003$. The s_o value was chosen to have a low bond breaking probability for improved material behavior analysis. The post-processor analysis was executed on 1000 values. Specifically, the analysis took into account a stretching range from $s_{min} = 0$ to $s_{max} = 3 \cdot 10^{-2}$, in order to better evaluate and analyze the amount of broken bonds.

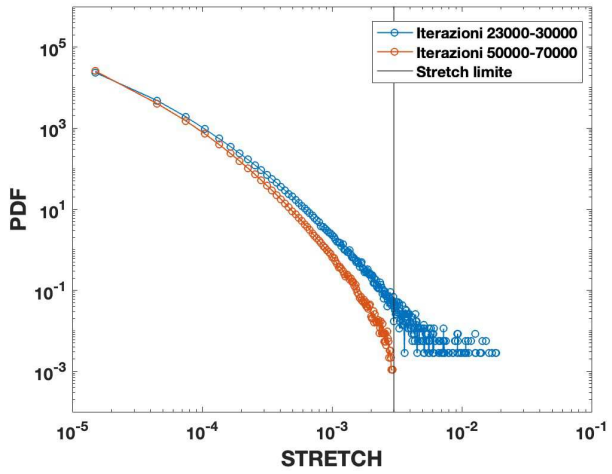

Figure 3.8: Graph related to the stretch obtained with the post-processor. The x-axis shows the strength values used, and the y-axis exhibits the probability distribution that corresponds to them.

The analysis consisted of two different ranges of iterations, first from 23000 to

30000, before the solid fracture was activated. The second step involves the activation of the fracture of the solid from iteration 50000 to iteration 70000. The examination conducted provides an estimate of break events following the activation of the solid fracture, which should be considered a qualitative analysis of the phenomenon taken into account. The graph 3.8 illustrates the results obtained, with the stretch values shown on the x-axis and the probability distribution displayed on the y-axis. As predicted, the graph shows that the probability of the event decreases as the stretch increases. In the graph, the blue line shows the values before the activation of solid fracture, and the orange line shows the values after the activation. The black line in the graph represents the assumed value of the stretch limit. According to the blue line, the stretches before activation of the fracture solid reach a higher value than the stretch limit, but with a lower probability than larger stretch values. As might be expected, the orange line still shows that the probability of events decreases as the stretching value increases. In this case, however, the probability of having a stretching greater than the limit value is zero, this is in agreement with the fact that the break of the solid has been activated. The bonds that exceeded the limit value have been broken and therefore they cannot be identified, as evidenced by the amplification in figure 3.9.

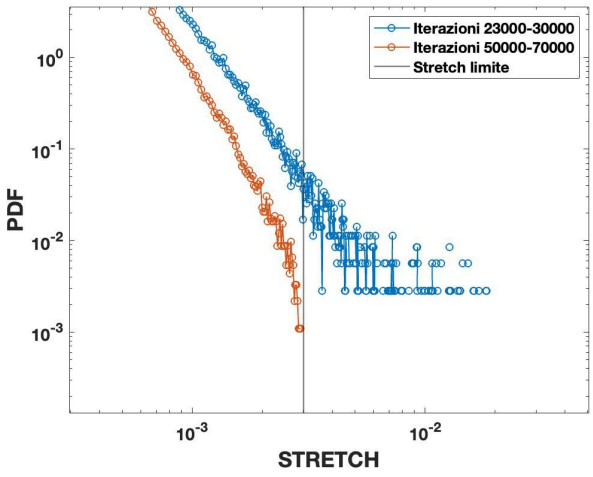

Figure 3.9: Magnification of the previous graph. Note that the values of the orange line do not exceed the stretching limit

After studying the stretches, tests were performed to analyze the stresses that were affecting the solid. Two trials were carried out with two distinct stress

ranges, resulting in the completion of the same iteration intervals employed for stretching. Post-processor stress was calculated using Von Mises' theory. The von Mises performance criterion is formulated in terms of von Mises stress or equivalent tensile strength. And von Mises failure criterion theory states that failure in any material occurs when the shear strain energy per unit volume stored in that material due to any loading exceeds the shear strain energy per unit volume stored in that material in the one-dimensional loading test (universal tensile test in the case of mild steel). Most of the ductile material failures can be predicted using von Mises criteria. Von Mises stress is calculated using the formula below:

$$\sigma_v = \sqrt{\frac{1}{2}\left[(\sigma_1 - \sigma_2)^2 + (\sigma_2 - \sigma_3)^2 + (\sigma_3 - \sigma_1)^2 + 6 \cdot (\sigma_{23}^2 - \sigma_{31}^2 - \sigma_{12}^2)\right]} \quad (3.3)$$

An estimate of the breaking tenion is also defined, obtained by the product between the limit bond stretch and the Young module (dimensional):

$$\sigma^*_{critical} = s_0 \cdot E = 133 \quad [\frac{N}{m^2}] \quad (3.4)$$

The graphs below show the pattern of stress acting on the material before and after the fracture in relation to the critical stress calculated by equation (3.4).

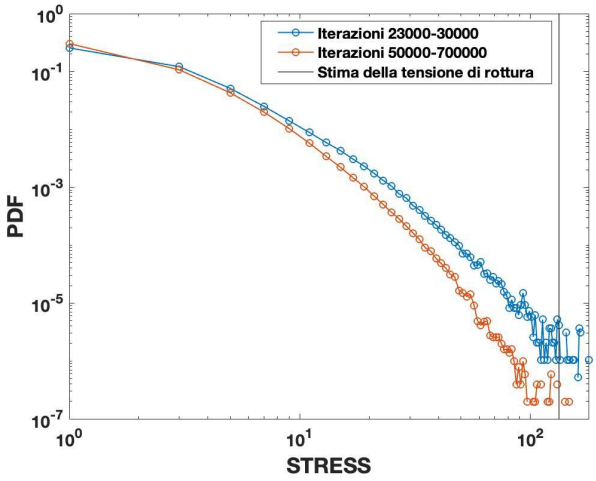

Figure 3.10: Magnification of the previous graph. Note that the values of the orange line do not exceed the stretching limit

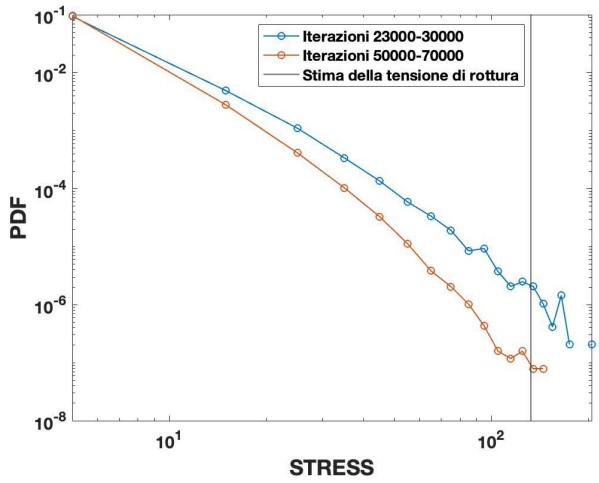

Figure 3.11: Magnification of the previous graph. Note that the values of the orange line do not exceed the stretching limit

The trend for 100 values is depicted in both images. Figure 3.10 is measured over a stress range of 0 to 200, and figure 3.11 covers a wider stress range of 0 to 1000. The stresses are represented by the x-axis and the probabilities are represented by the y-axis. As in the previous case, the blue line shows the results obtained before the activation of the fracture, while the orange line shows the trend after the activation of the latter. The black vertical line indicates the calculated critical stress. Based on these two graphs, it can be concluded that the stress on the material decreases after the fracture is activated. In terms of quality, it is what was expected. Activation causes the bonds between particles in the peridynamic solid to break, resulting in a decrease in the tension acting on the material. The bonds reach their deformation and their intrinsic energy limit, which leads to their break. It can also be noted that there is a low probability of events exceeding critical stress. The bonds can reach the limit stress prior to activation, and as per figure 3.9 of the stretch, they have the potential to deform beyond the maximum stretching, but with a low probability. The deformation energy did not account for in this case. In the second scenario, when considering the activation of the energy fracture release rate, the figures 3.1 and 3.12 demonstrate that external forces can cause greater stress than of the material limit stress, with a very small probability of 10^{-7}, but the bonds are fully broken. It can therefore be concluded that the material behaves, qualitatively, as expected. Bonds that accumulate more energy than they can

sustain, due to the action of fluid external forces, break. As a result, there is a decrease in tension.

CHAPTER 4

Conclusion and future developments

Fluid-Structure Interaction (FSI) is a very complex phenomenon and its study in the most varied fields of engineering is still a challenge. In this thesis, the preliminary study of the breakup of a fibrous ablative porous solid in a laminar flow is presented. The analysis was performed by using the code developed by F. Dalla Barba, which is based on the open-source software CaNS of P.Costa and allows for DNS to be performed. The software discretizes the Navier-Stokes equations in an incompressible form and implements peridynamic theory to represent solid materials. The important benefit of this theory is that it provides an intrinsic representation of fracture and crack propagation, without the need to incorporate additional models in the computational code. All the analyses were carried out in non-dimensional form to study the phenomenon of fracture. After determining the proper parameters and carrying out a simulation in which the solid fibers composing the solid medium were broken, the analysis focused on determining the probability distribution of stretches and stresses. In this simulation, the stress on the fibers was calculated according to Von Mises's theory. The values obtained were compared between the fibers in which the fracture phenomenon occurs and then with fibers in which the fracture does not occur, to compare the orders of magnitude of the respective stresses (in non-dimensional form) between them. After achieving this goal, more implementation cycles could be considered as possible solutions for the future development of this study. The solid is not completely broken. Analyzing the stretches and stresses on the individual fibers can allow for the study of the material's cycles and fatigue life.

Bibliography

[1] Yuri Bazilevs, Kenji Takizawa, and Tayfun E Tezduyar. *Computational fluid-structure interaction: methods and applications*. John Wiley & Sons, 2013.

[2] A Bobet, A Fakhimi, Scott Johnson, Joseph Morris, Fulvio Tonon, and M Ronald Yeung. Numerical models in discontinuous media: review of advances for rock mechanics applications. *Journal of geotechnical and geoenvironmental engineering*, 135(11):1547–1561, 2009.

[3] Wim-Paul Breugem. A second-order accurate immersed boundary method for fully resolved simulations of particle-laden flows. *Journal of Computational Physics*, 231(13):4469–4498, 2012.

[4] Tuanny Cajuhi, Lorenzo Sanavia, and Laura De Lorenzis. Phase-field modeling of fracture in variably saturated porous media. *Computational Mechanics*, 61:299–318, 2018.

[5] Pedro Costa. A fft-based finite-difference solver for massively-parallel direct numerical simulations of turbulent flows. *Computers & Mathematics with Applications*, 76(8):1853–1862, 2018.

[6] F Dalla Barba and F Picano. A new method for fully resolved simulations of fracturing in fluid-structure interaction problems. In *Direct and Large Eddy Simulation XII*, pages 469–475. Springer, 2020.

[7] F Dalla Barba and F Picano. A novel approach for direct numerical simulation of hydraulic fracture problems. *Flow, Turbulence and Combustion*, 105:335–357, 2020.

[8] F Dalla Barba, P Campagnari, M Zaccariotto, U Galvanetto, and F Picano. A fluid-structure interaction model based on peridynamics and navier–stokes equations for hydraulic fracture problems. In *7th European Conference on Computational Fluid Dynamics, Glasgow, UK*, 2018.

[9] Federico Dalla Barba and Francesco Picano. Direct numerical simulation of the scouring of a brittle streambed in a turbulent channel flow. *Acta Mechanica*, 232:4705–4728, 2021.

[10] Marco D de Tullio and Giuseppe Pascazio. A moving-least-squares immersed boundary method for simulating the fluid–structure interaction of

elastic bodies with arbitrary thickness. *Journal of Computational Physics*, 325:201–225, 2016.

[11] Daniele Dipasquale, Mirco Zaccariotto, and Ugo Galvanetto. Crack propagation with adaptive grid refinement in 2d peridynamics. *International Journal of Fracture*, 190:1–22, 2014.

[12] L Hedjazi, CL Martin, S Guessasma, G Della Valle, and R Dendievel. Application of the discrete element method to crack propagation and crack branching in a vitreous dense biopolymer material. *International Journal of Solids and Structures*, 49(13):1893–1899, 2012.

[13] Cyrill W Hirt, Anthony A Amsden, and JL Cook. An arbitrary lagrangian-eulerian computing method for all flow speeds. *Journal of computational physics*, 14(3):227–253, 1974.

[14] Gene Hou, Jin Wang, and Anita Layton. Numerical methods for fluid-structure interaction—a review. *Communications in Computational Physics*, 12(2):337–377, 2012.

[15] Harald Kruggel-Emden, Erdem Simsek, Stefan Rickelt, Siegmar Wirtz, and Viktor Scherer. Review and extension of normal force models for the discrete element method. *Powder Technology*, 171(3):157–173, 2007.

[16] QV Le and Florin Bobaru. Surface corrections for peridynamic models in elasticity and fracture. *Computational Mechanics*, 61:499–518, 2018.

[17] Richard W Macek and Stewart A Silling. Peridynamics via finite element analysis. *Finite elements in analysis and design*, 43(15):1169–1178, 2007.

[18] SEYED HOSSEIN Madani, J Wissink, and HAMID Bahai. Acomparision of conforming and non-conforming mesh methods for flow around a circular cylinder in non-inertial frame of references. In *COUPLED VI: proceedings of the VI International Conference on Computational Methods for Coupled Problems in Science and Engineering*, pages 1037–1046. CIMNE, 2015.

[19] Erdogan Madenci and Erkan Oterkus. Peridynamic theory. In *Peridynamic theory and its applications*, pages 19–43. Springer, 2013.

[20] Rajat Mittal and Gianluca Iaccarino. Immersed boundary methods. *Annu. Rev. Fluid Mech.*, 37:239–261, 2005.

[21] Sumant R Morab and Atul Sharma. An overview of computational fluid structure interaction: Methods and applications. *arXiv preprint arXiv:2006.04068*, 2020.

[22] Mohammad Rezanezhad, Seyed Ahmad Lajevardi, and Sadegh Karimpouli. An investigation on prevalent strategies for xfem-based numerical modeling of crack growth in porous media. *Frontiers of Structural and Civil Engineering*, 15:914–936, 2021.

[23] Alexandre M Roma, Charles S Peskin, and Marsha J Berger. An adaptive version of the immersed boundary method. *Journal of computational physics*, 153(2):509–534, 1999.

[24] Ruben Scardovelli and Stéphane Zaleski. Direct numerical simulation of free-surface and interfacial flow. *Annual review of fluid mechanics*, 31(1): 567–603, 1999.

[25] Mohamed Shaat, Esmaeal Ghavanloo, and S Ahmad Fazelzadeh. Review on nonlocal continuum mechanics: physics, material applicability, and mathematics. *Mechanics of Materials*, 150:103587, 2020.

[26] Stewart A Silling. Reformulation of elasticity theory for discontinuities and long-range forces. *Journal of the Mechanics and Physics of Solids*, 48 (1):175–209, 2000.

[27] Stewart A Silling and Ebrahim Askari. A meshfree method based on the peridynamic model of solid mechanics. *Computers & structures*, 83 (17-18):1526–1535, 2005.

[28] Stewart A Silling and Richard B Lehoucq. Convergence of peridynamics to classical elasticity theory. *Journal of Elasticity*, 93:13–37, 2008.

[29] Stewart A Silling and Richard B Lehoucq. Peridynamic theory of solid mechanics. *Advances in applied mechanics*, 44:73–168, 2010.

[30] Stewart A Silling, M Epton, Olaf Weckner, Jifeng Xu, and E23481501120 Askari. Peridynamic states and constitutive modeling. *Journal of elasticity*, 88:151–184, 2007.

[31] Mohamed Souli, A Ouahsine, and L Lewin. Ale formulation for fluid–structure interaction problems. *Computer methods in applied mechanics and engineering*, 190(5-7):659–675, 2000.

[32] Vamsi Spandan, Valentina Meschini, Rodolfo Ostilla-Mónico, Detlef Lohse, Giorgio Querzoli, Marco D de Tullio, and Roberto Verzicco. A parallel interaction potential approach coupled with the immersed boundary method for fully resolved simulations of deformable interfaces and membranes. *Journal of computational physics*, 348:567–590, 2017.

[33] N Sukumar, JE Dolbow, and Nicolas Moës. Extended finite element method in computational fracture mechanics: a retrospective examination. *International Journal of Fracture*, 196:189–206, 2015.

[34] Natarajan Sukumar, Nicolas Moës, Brian Moran, and Ted Belytschko. Extended finite element method for three-dimensional crack modelling. *International journal for numerical methods in engineering*, 48(11):1549–1570, 2000.

[35] Markus Uhlmann. An immersed boundary method with direct forcing for the simulation of particulate flows. *Journal of computational physics*, 209 (2):448–476, 2005.

[36] Shizhao Wang, Marcos Vanella, and Elias Balaras. A hydrodynamic stress model for simulating turbulence/particle interactions with immersed boundary methods. *Journal of Computational Physics*, 382:240–263, 2019.

[37] TT Yu. The extended finite element method (xfem) for discontinuous rock masses. *Engineering Computations*, 28(3):340–369, 2011.

[38] Francisco Zárate and Eugenio Oñate. A simple fem–dem technique for fracture prediction in materials and structures. *Computational particle mechanics*, 2:301–314, 2015.